Sediment dynamics on the outer-shelf of the Gulf of Lions during a storm: An approach based on acoustic glider and numerical modeling

Mathieu Gentil, Claude Estournel, Xavier Durrieu de Madron, Gaël Many, Travis Miles, Patrick Marsaleix, Serge Berné, François Bourrin

▶ **To cite this version:**

Mathieu Gentil, Claude Estournel, Xavier Durrieu de Madron, Gaël Many, Travis Miles, et al.. Sediment dynamics on the outer-shelf of the Gulf of Lions during a storm: An approach based on acoustic glider and numerical modeling. CONTINENTAL SHELF RESEARCH, 2022, 240, 10.1016/j.csr.2022.104721 . insu-03671372

HAL Id: insu-03671372
https://insu.hal.science/insu-03671372

Submitted on 22 Jul 2024

HAL is a multi-disciplinary open access archive for the deposit and dissemination of scientific research documents, whether they are published or not. The documents may come from teaching and research institutions in France or abroad, or from public or private research centers.

L'archive ouverte pluridisciplinaire **HAL**, est destinée au dépôt et à la diffusion de documents scientifiques de niveau recherche, publiés ou non, émanant des établissements d'enseignement et de recherche français ou étrangers, des laboratoires publics ou privés.

Distributed under a Creative Commons Attribution - NonCommercial 4.0 International License

Version of Record: https://www.sciencedirect.com/science/article/pii/S0278434322000759
Manuscript_efd5e4971d7bd0e817dfe051538de2b5

Continental Shelf Research 240 (2022) 104721

Contents lists available at ScienceDirect

Continental Shelf Research

journal homepage: www.elsevier.com/locate/csr

Sediment dynamics on the outer-shelf of the Gulf of Lions during a storm: An approach based on acoustic glider and numerical modeling

Mathieu Gentil [a,*], Claude Estournel [b], Xavier Durrieu de Madron [a], Gaël Many [c], Travis Miles [d], Patrick Marsaleix [b], Serge Berné [a], François Bourrin [a]

[a] CEFREM, CNRS, Université de Perpignan Via Domitia, 52 Avenue Paul Alduy, 66860, Perpignan, France
[b] LEGOS, Université de Toulouse, CNES, CNRS, IRD, UPS, Toulouse, France
[c] IDYST, Université of Lausanne, Switzerland
[d] Rutgers, The State University of New Jersey, New Brunswick, NJ, USA

ARTICLE INFO

Keywords:
Storm event
Wave-current interaction
Sediment dynamics
Acoustic-glider
Hydrodynamic and wave models
Gulf of lions
Mediterranean

ABSTRACT

Describing and quantifying storm-induced sediment dynamics enables improved mapping of the fate of sediments over continental shelves, which is necessary to understand their role in the structure and dynamics of marine ecosystems, nutrient cycling, and dispersion of pollutants. Storms are episodic processes that can lead to massive sediment resuspension and transport on continental shelves. However, understanding sediment dynamics during storms remains a challenge, because these events are spatially under-sampled due to their intermittency and intensity. This paper quantifies processes that drive sediment dynamics and their spatiotemporal variability over the outer shelf of the Gulf of Lions (NW Mediterranean), during a 5-year return period storm, using an active acoustic glider combined with a hydrodynamic model (SYMPHONIE) and wave model (WAVEWATCH-III). The glider-ADCP (Acoustic Doppler Current Profiler) measurements proved invaluable validation of current vertical profiles of the hydrodynamic model during this episodic event. The combination of observations with numerical simulations suggest that sediment resuspension is an important process at depths greater than 90 m on the shelf. This appears to be primarily due to the wave forcing, which most likely accounts for some of the observed increase in suspended particulate matter in the water column. At the regional scale, an along shelf sediment transfer by successive jumps associated with onshore storms is suggested, from the main input (the Rhone River) to the output (the Cap de Creus) area of the Gulf of Lions' shelf. This study highlights the complementarity between numerical modeling and new observation instrument designed to spatially extend the measurement of current and turbidity to study sediment resuspension and transport during extreme events on continental shelves.

1. Introduction

1.1. Coastal storm and sediment dynamics

Sediment dynamics over continental shelves are strongly influenced by multiple forcings (river flows, currents, winds, waves), among which storm-induced mixing events are particularly important episodic processes (Nittrouer et al., 2007). Both waves and currents can generate bottom shear stress that can result in potentially massive sediment resuspension, through non-linear interactions (Grant and Madsen, 1979; Soulsby et al., 1993; Van Rijn and Kroon, 1993). However, describing and quantifying sediment resuspension and transport on continental shelves during storms remains a challenge because of the extreme spatial and temporal variability of their effects on hydrodynamics and sediments. Enriching the documentation of the hydro-sedimentary conditions that control sediment resuspension and transport are crucial to predict the fate of sediment and pollutants that are introduced onto the shelf and which might be reworking and off-shelf export (Olsen et al., 1982; Kane and Clare, 2019).

Most *in-situ* observations of wave-current interactions and sediment resuspension are gathered at few fixed locations on the shelf, from optical and acoustic sensors on tripods and benthic landers (Chang et al., 2001; Drake et al., 1992; Drake and Cacchione, 1986; Jing and Ridd, 1996; Liu et al., 2017; Niu et al., 2020; Palinkas et al., 2010). Such

* Corresponding author.
E-mail address: mathieu.gentil@univ-perp.fr (M. Gentil).

https://doi.org/10.1016/j.csr.2022.104721
Received 21 October 2021; Received in revised form 18 February 2022; Accepted 4 April 2022
Available online 7 April 2022
0278-4343/© 2022 Elsevier Ltd. All rights reserved.

© 2022 published by Elsevier. This manuscript is made available under the CC BY NC user license
https://creativecommons.org/licenses/by-nc/4.0/

observations provide precise information on the temporal variability of the bottom layer dynamics but do not capture the spatial gradients across the entire shelf or evaluate the overall sediment transport. To fill this gap and understand sediment dynamics at regional scales, three-dimensional hydrodynamic models have been used (Dalyander et al., 2013; Dufois et al., 2008; King et al., 2019; Styles and Glenn, 2005; Ulses et al., 2008a). However, these studies face the difficulty of modeling hydrodynamic parameters under extreme conditions as well as sediment behavior in a wide range of sand-mud mixtures associated with a variety of complex bedforms. In this context, the combination of numerical modeling and new autonomous ocean observing technologies designed to spatially extend the measurement of sediment dynamics appears promising (Miles et al., 2015).

Underwater gliders are becoming increasingly important for the collection of oceanographic measurements in observing programs (Liblik et al., 2016; Rudnick, 2016; Testor et al., 2019). These systems are low power long-term duration (>30 days) autonomous underwater vehicles that can carry a range of interchangeable sensor packages and sample the water column on large spatial scales (>100 km). Several studies have shown the ability of autonomous gliders equipped with physical and optical sensors to study the spatial and temporal variability of sediment resuspension on continental shelves, especially in stormy conditions (Bourrin et al., 2015; Glenn et al., 2008; Many et al., 2018; Miles et al., 2013, 2021). The recent integration of Acoustic Doppler Current Profilers (ADCPs) onto gliders allows for accurate descriptions of currents throughout the water column along their trajectory, essential to understand physical processes that occur during storms and to quantify sediment transport on continental shelves (Gentil et al., 2020; Miles et al., 2015).

During the last decades, the GoL has been targeted by numerous observational programs dealing with the present-day particle flux dynamics (Durrieu de Madron et al., 2008; Weaver et al., 2006). However, the outer shelf has almost never been directly sampled, especially during storms, using classical Eulerian methods (such as bottom tripods) because of the risks associated with intense trawling activities (Ferré et al., 2008). This observational gap is detrimental to the understanding of sediment dynamics on a large part of the shelf and incidentally on the validation of hydrodynamic and sediment dynamics models. Here we present a study combining glider observations and modeling approach to characterize processes responsible for sediment resuspension and to quantify sediment transport during a marine storm in the Gulf of Lions (GoL) shelf in the north-western Mediterranean.

1.2. The Gulf of Lions

1.2.1. Sediment features

Sediment source on the GoL shelf is essentially dependent upon suspended matter inputs from the Rhone River (8.4 Mt yr^{-1} +/− 4.5 t yr^{-1}) in the northeast, and to a lesser extent to several small rivers along the central and western part of the Gulf (Sadaoui et al., 2016). The shelf presents contrasted sedimentological features (Aloısi, 1986; Berne et al., 1998; Monaco, 1971) (Fig. 1a) with: (i) a sandy inner shelf (<30 m), (ii) a mid shelf mud-belt (30–90 m) characterized by deposition of cohesive sediments mainly from the Rhone River, and (iii) coarser sediments with muddy sand patches on the outer shelf (>90 m).

Muddy sands of the outer shelf are homogeneous and bioturbated

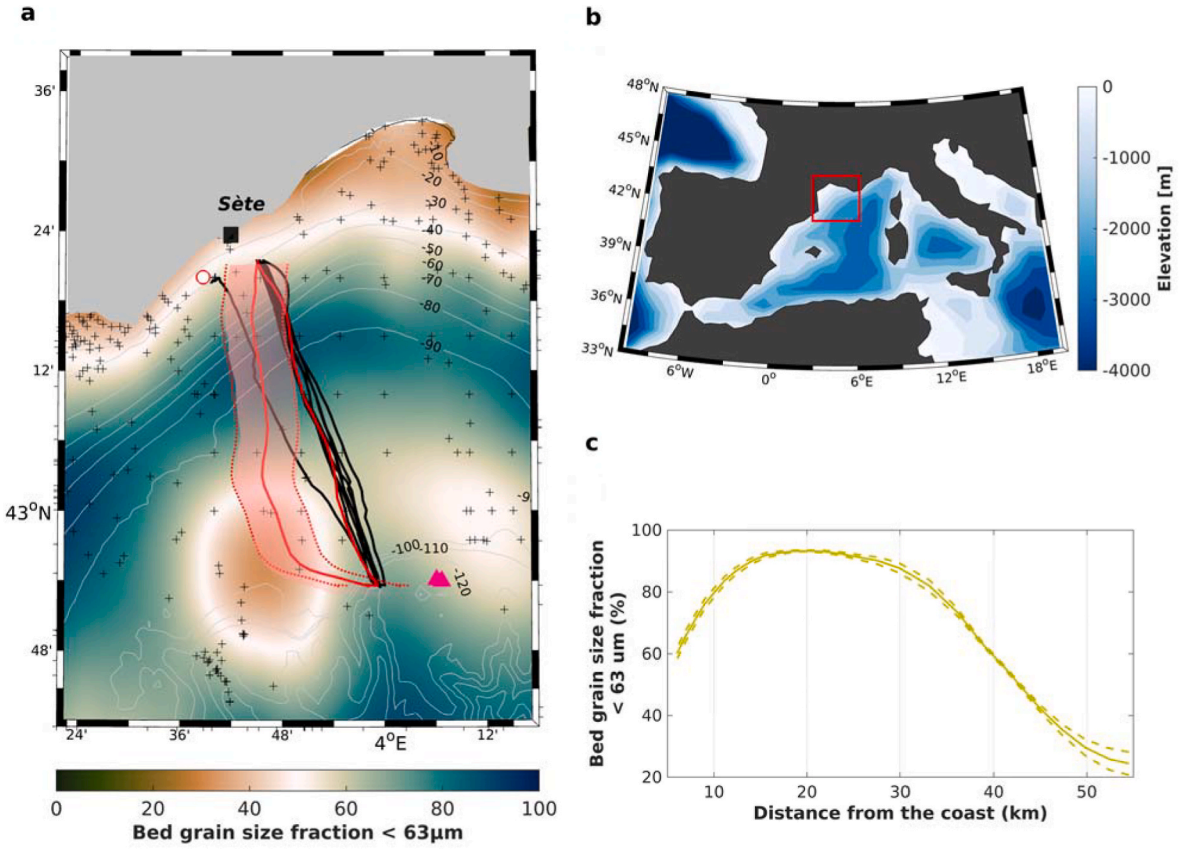

Fig. 1. (a) Map of the glider track (solid black and red lines) superimposed on shelf surface sediment characteristics of the central part of the Gulf of Lions, interpolated from the granulometric samples (black crosses). The location of the coastal buoy (red and white circle), the meteorological station (black square), and the bedform images of Fig. 2 (pink triangles) are also shown. The solid red lines indicate the two glider sections of interest for this study. (b) General map of western Mediterranean, where the Gulf of Lions is located by a Red Square. (c) Content of fine sediment (<63 µm) (solid green line) in bottom sediment as a function of the distance from the coast. Uncertainty on the pelitic fraction (dashed green line) has been derived from interpolated surface sediment characteristics (red-shaded area in Fig. 1a) along the glider section during storm conditions.

(Bassetti et al., 2006), as shown by Fig. 2. The sandy fraction corresponds to relict "offshore sands", which cover many continental shelves around the world, at water depths generally between 80 and 120 m (Emery, 1968). These sediments represent littoral relict formations from the last eustatic low stage that were reworked during the first phase of the eustatic sea-level rise (Bassetti et al., 2006; Berne et al., 1998; Perez Belmonte, 2003). In this part of the shelf, sand ripples and large bedforms (dunes) are often found as reported by Bourcart (1945) and Bassetti et al. (2006). The muddy fraction has a more recent origin and is mainly sourced from the Rhone River. In the GoL, mixed sandy mud sediments may be remobilized from the outer shelf and supply sediments to canyon heads (Gaudin et al., 2006). Understanding the evolution of these deposits requires taking into account present-day sediment dynamics.

1.2.2. Hydrodynamic features

The GoL is a low-energy wave-dominated area (Guizien, 2009), where tides have small amplitudes (a few cm) and associated currents are very weak of a few mm s^{-1} (Carrère et al., 2012). Various observational (Bonnin et al., 2008; Bourrin et al., 2008, 2015; Ferré et al., 2005; Guillén et al., 2006; Martín et al., 2013; Ogston et al., 2008; Palanques et al., 2006, 2008) and modeling (Dufois et al., 2008; Ferré et al., 2008; Ulses et al., 2008b) studies emphasized the role of severe E-SE storms on the resuspension and redistribution of the shelf sediments. The E-SE storms have a marked seasonal impact with a maximum occurrence during autumn and winter (Mikolajczak et al., 2020).

Coastal buoys have shown that during storms, sediment resuspension is primarily driven by waves for depths <30 m (Guillén et al., 2006; Pruski et al., 2019). However, such events are very difficult to observe over the shelf, mainly because of the difficulties of maintaining equipment in such regions exposed to trawling activities. To fill these gaps, modeling studies were carried out to gain an insight into the hydro-sedimentary processes on the coastal continuum. Ulses et al. (2008b) showed, for an east storm event, that the influence of waves on resuspension on the outer shelf can be neglected in contrast to strong near-bottom currents that may generate resuspension. However, Dufois et al. (2008) showed from a 1-year simulation that waves can generate a maximum bottom shear stress of 0.08 N m^{-2} over depths of 100 m for severe E-SE storms. These conclusions are shared by Palanques et al. (2008), who found wave shear stresses higher than 0.12 N m^{-2} from extrapolation between observations recorded on the inner shelf and the canyon head during a marine storm.

Given the diversity of storms, the few existing studies targeting some of them are not sufficient to fully understand resuspension and advection processes during these episodic events. There is a lack of measurements in the coastal continuum, especially on the mid and outer shelf. Bourrin et al. (2015) used a glider equipped with physical and optical sensors to detail and quantify cross-shelf sediment dynamics induced by a storm on the Catalan shelf (southwestern part of the GoL). However, the instruments used in this study did not allow the quantification of baroclinic conditions in the water column and their impact on resuspension.

The present work builds on the aforementioned papers. It describes a comprehensive set of observations collected on the shelf coupled with hydrodynamic modeling used to study the fate of muddy sands on outer continental shelves. The methods and tools used to characterize hydro-sedimentary processes under storm events are described in section 2. Section 3 then presents the physical processes driving the sediment resuspension, and transport on a muddy sand outer shelf. Finally, the glider-ADCP contribution to describe the episodic events and their impact on the spatiotemporal variability of sediment dynamics is discussed in section 4.

2. Data and methods

2.1. Glider observation

2.1.1. Sampling strategy

A glider equipped with a CTD (Conductivity, Temperature, Depth), an optical payload, and an ADCP was deployed in the central part of the GoL (Fig. 1a) in February–March 2018. The sampling strategy was adapted to target a continuous observation period of more than 30 days to sample short-term energetic events. In total, 11 cross-shelf sections were carried out from the mid shelf (5 km offshore to 30 m depth) to the shelf edge (55 km offshore to 100 m depth) (Fig. 1a). Each section was generally performed in 2.5–3 days, with an average of 222 yos (down/up-casts) by transect. This long deployment permitted monitoring of a storm event on the shelf from 1st to March 2, 2018.

2.1.2. Glider system and sensors

In this study, we used a Teledyne Webb Research Slocum G1 autonomous underwater glider with an operating range of 30–200 m water depth (Davis et al., 2002). The glider is driven primarily through small changes in buoyancy that allow it to "glide" forward through the water column on the descent, to typically 2 m above bottom, and ascend to 0–1 m from the surface. The chosen settings allowed the glider to descend and ascend through the water column with a pitch angle of approximately 26°, and horizontal and vertical speeds of 0.3 and 0.15 m s^{-1}, respectively. The glider surfaced every six down- and up-casts (yos) to obtain GPS fixes and transfer data to land, and to receive any new information about its route configuration and sampling strategy.

The glider was equipped with a suite of sensors that allow for continuous monitoring of physical and chemical characteristics of the whole water column. Conductivity, temperature, and pressure measurements were made using a pumped SeaBird 41cp CTD. An optical backscatter sensor (ECO-FLNTU) provided light scattering at 700 nm calibrated in NTU (Normalized Turbidity Units) and the fluorescence of chlorophyll-a. Using a sampling frequency of 0.5 Hz and a fall speed of approximately 0.15 m s^{-1}, the glider collects ~3 measurements per meter from all sensors yielding a detailed look at the water column vertical structure. An Explorer Doppler Velocity Log with Acoustic Doppler Current Profiling capacity (Explorer ADCP) at 614 kHz was integrated into a special payload bay on the Slocum glider. It measures water column currents, the velocity of the glider and also the acoustic backscatter intensity. The Explorer ADCP has a downward-facing transducer tilted 11° forward, which enables it to compensate for the pitch of the glider during downcast. The inclination of the transducer optimized the three-beam measurements on the 26° pitched glider during the downcast. This fixed forward configuration rendered the instrument unsuitable for collecting velocity profile data during upcast (Mullison et al., 2013). Dedicated high accuracy attitude and compass sensors were used by the ADCP to monitor the beam orientation and were calibrated before deployment, following the procedure of PNI Sensor Corporation (2013). During a glider descent, the ADCP periodically recorded echo intensity and relative water velocities to a maximum range of 20 m. A sampling frequency of 0.33 Hz was set to optimize the duration of the glider deployment. This sampling frequency (ensemble of 3 pings every 10 s) allowed sampling of profiles spaced on average every 1.2 m along the glider trajectory and 0.6 m vertically.

2.1.3. Glider data processing

Science and navigation data—During surfacing, the glider used GPS positioning to estimate the difference between the expected surface location from underwater dead reckoning and the GPS fixes. Such position difference, dependent on the duration of the dive, allowed for the estimation of the depth-averaged current (DAC) between two surfacings (Eriksen et al., 2001; Rudnick et al., 2018). Conductivity and temperature measurements were corrected for thermal lag effects (Garau et al., 2011). Salinity, density, and Brunt-Väisälä frequency were derived using the TEOS-10 equation (McDougall and Barker, 2011). CTD and optical measurements were synchronized with ADCP data and interpolated to a periodicity of 4 s.

Acoustic data—The Explorer ADCP data were processed to retrieve the Backscatter Index (BI) from echo intensities and absolute velocities from relative velocities using the method detailed in Gentil et al., (2020). ADCP measurements were organized along a diagonal swath, with overlapping measurements at each depth (see Fig. 3 in Gentil et al., 2020). For echo intensity measurements, a correction was applied on cell depths to avoid the effect of the pitched transducer (Ordonez et al., 2012). The real depth of each cell was thus calculated, taking into account the pitch and roll effects, the blanking distance, and the depth of the glider. Finally, to properly estimate the backscatter index and the relative water velocities, the factory threshold of 64 counts of the correlation signal was used to remove the noise floor values (Gordon, 1996).

The received level of the acoustic return along each beam was converted into BI (dB) using equations of Mullison (2017), derived from the work of Gostiaux and van Haren (2010), and Deines (1999). BI is estimated from the correction of the received echo intensity by (i) the noise level, (ii) a calibration factor from counts (instrumental unit) to decibels, (iii) the loss due to absorption by seawater, and (iv) the loss due to spherical spreading. The main advantage of the formula proposed by Mullison (2017), is the estimation of absolute value of the acoustic backscatter (dB), whatever the environment even those known for their low concentration of backscatter. Then, the successive profiles of the BI were stacked into bins of 2 m, to reconstruct the profile over the entire water column from the median values of the overlapping data at each level. A final three-point centered moving-average filter was applied to eliminate the high-frequency noise.

Velocities used in this work were converted from beam coordinates to Earth coordinates and were bin-mapped using ADCP attitude sensor outputs. ADCP measurements combine glider motion with current velocity. Absolute water velocities were derived using the shear method (de Fommervault et al., 2019; Fischer and Visbeck, 1993; Gentil et al., 2020). The shear method is based on the assumption that glider speed is constant for each individual profile and is, therefore, eliminated when estimating the vertical shear of the velocity for each profile. After reconstructing the shear of the current over the whole water column, its integration allows to obtain a relative water velocity profile. The integration constant corresponding to a barotropic velocity component is required in order to derive absolute water velocities profiles. This barotropic component was estimated from the DAC, because the bottom track measurements showed erroneous values, probably due to an acquisition problem. The different steps of the shear method were applied independently to E-W and N–S components to (i) calculate single-ensemble shear by vertically differentiating ADCP velocity profiles; (ii) grid the resulting shear estimates in depth space (median values of shear current per 2 m cell); (iii) vertically integrate shear to yield the relative velocity profile, and (iv) estimate absolute velocities by adjusting relative velocity profiles to the current velocities measured by DAC. Estimation of velocity started at a depth of 3 m, due to the position of the ADCP under the glider and a blanking distance of 2 m.

Uncertainty in BI profiles corresponds to the standard deviation of the stacked values for each 2 m depth bin. For relative velocity, the standard deviation of single ping measurements for 2 m cell size at 614 kHz is about 0.03 m s^{-1} (Gordon, 1996). To estimate the uncertainty of the relative velocity estimates, we performed a Monte-Carlo simulation based on 500 iterations, with initial velocity values sampled randomly according to a normal distribution centered on the measured value for each bin of each profile during the downcast. Finally, an average standard deviation of the absolute velocity—calculated from the sum of variances of the relative velocities and the DAC—was estimated at 0.06 m s^{-1}.

2.2. Additional observation assets

Geological Settings—A surface sediment map of the shelf was determined by interpolating sediment samples (black crosses in Fig. 1a) on a regular grid of 100 m, using the data-interpolating variational analysis (DIVA) method (Troupin et al., 2012). Sediment samples were compiled from numerous grab samples and piston cores acquired over the last ca. 40 years, as part of French and European projects (Augris et al., 2013). The resulting surface sediment map is very similar to the distribution described by Got and Aloisi (1990). In the vicinity of the glider track, close examination of sediment samples suggests a representative median grain size between 10 and 30 μm for the mid shelf, whereas the outer shelf has a representative median grain size between 40 and 70 μm, and is composed of muddy sands (Bassetti et al., 2006). Uncertainty about the pelitic fraction has been estimated from the median of the interpolated sediment characteristics (Fig. 1c) over a 5 km band on both sides of the glider track (red shaded area in Fig. 1a). Fig. 2 shows photos of the bedform and the biological stands on the outer shelf of the GoL, at the vicinity of the study area (pink triangles in Fig. 1a).

Coastal buoy time series—Waves were monitored at 30 m water depth (43 °22.261′N; 3°46.777′E) (red and white circle in Fig. 1a), every 30 min with a directional wave buoy (Datawell®). The main wave characteristics (significant and maximum height, mean period, and direction) were retrieved from the CANDHIS database (http://candhis.cetmef.developpement-durable.gouv.fr).

Meteorological time series—Hourly (10 min burst average) wind speed and direction were measured at the Météo-France Sète station (34,301,002) located at 43 °23.50′N; 3°41.31′E (black square in Fig. 1a). Data were provided by MeteoFrance and are available in the Publithèque database (https://donneespubliques.meteofrance.fr/).

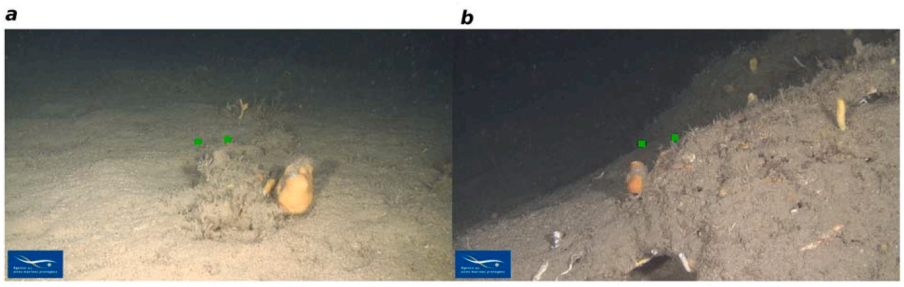

Fig. 2. Seabed images (Agence des aires marines protégées et al., 2012) of bioturbated muddy sands over the outer shelf of the Gulf of Lions (characterized by yellow patches in Fig. 1a). (a) orange sponges at 96 m depth. (b) Echnis, bonelia, orange and yellow sponges and alcyons at 105 m depth. The seabed images (a) and (b), located at 42 °53.059′N; 4°04.162′E and 42 °53.066′N; 4°04.125′E respectively (pink triangles in Fig. 1a), are outside the study area but close enough to consider that the particle characteristics are similar. The spacing between the green markers is 10 cm.

2.3. Hydrodynamical modeling

The 3-D ocean circulation model SYMPHONIE (Marsaleix et al., 2008, 2019) is based on the Navier-Stokes primitive equations solved on an Arakawa horizontal curvilinear C-grid and a VQS vertical coordinate (Estournel et al., 2021), under the hydrostatic and Boussinesq approximations. The model makes use of an energy-conserving finite difference method described by Marsaleix et al. (2008), a forward-backward time stepping scheme, a Jacobian pressure gradient scheme (Marsaleix et al., 2009), the equation of state of Jackett et al. (2006), and the K-epsilon turbulence scheme implemented following Michaud et al. (2012). The lateral open boundary conditions, based on radiation conditions combined with nudging conditions, are described in Marsaleix et al. (2006). The bipolar horizontal grid is the same as that of Mikolajczak et al. (2020)—see their Fig. 1b—with a resolution between 300 and 500 m over the entire GoL continental shelf. The vertical VQS grid has 40 levels in total and about 20 on the continental shelf to reduce truncation errors associated with the sigma coordinate while maintaining an accurate description of the bathymetry. A particularly important property of this coordinate for this study is that it preserves the horizontal continuity of the bottom current (i.e., without the blocking effect of staircase coordinates). Among the numerous applications of SYMPHONIE in the Mediterranean, simulations targeting wind-induced circulation on the GoL' shelf have been analyzed and validated by Estournel et al. (2003) and Petrenko et al. (2008).

The simulation is a downscaling from a lower resolution simulation of the entire Mediterranean Basin carried out with the SYMPHONIE model (Estournel et al., 2021; see their Fig. 6 for comparison with the average SST in January 2018). The forcing at the air/sea interface is done by the COARE3.0 bulk formulas fed by ECMWF hourly forecasts. Taking into account the recommendations of Van Sebille et al. (2020) regarding the effects of waves on transport, a simplified parameterization of the effect of waves on currents is introduced into the model. This parameterization, similar to that of McWilliams and Restrepo (1999) and Jorda et al. (2007), only retains the leading terms of the current/-wave interactions (i.e., neglecting the quadratic terms, the Vortex force in particular). The horizontal components of the Stokes drift (u_s, v_s), are in practice added to the Eulerian current for the calculation of advection and the transport divergence giving the variation of the surface elevation. As described by Jorda et al. (2007), the modified momentum equations add the Stokes-Coriolis force (Van Sebille et al., 2020; Xu and Bowen, 1994) to the Coriolis term (i.e. $+fu\rightarrow +f(u, u_s)$ and $-fv\rightarrow -f(v, vu_s)$). Finally, similarly to Jorda et al. (2007), a wave-induced increase of the bottom stress is applied (see section 2.5.5 Eq. (9)). The characteristics of waves are interpolated in space and time from the fields obtained with the WAVEWATCH-III model (section 2.4).

The simulation is initialized on December 13, 2017 and runs until the storm studied here (early March 2018).

2.4. Wave modeling

The wave characteristics (significant height, period, direction, and Stokes drift) are calculated with the WAVEWATCH-III wave generation and propagation model (Tolman, 2009) using the grid of the parent model (see above) throughout the Mediterranean. The model is forced by the wind using the same product as above (ECMWF wind). Outputs are archived hourly.

2.5. Diagnostics

Glider data have been analyzed in the context of other available datasets such as coastal buoys, granulometric samples, meteorological time series, and hydrodynamic modeling. Diagnostics were implemented to characterize hydrometeorological events, the suspended particulate matter properties, the physical processes that drive sediment dynamics in the bottom boundary layer, and their transport across the GoL shelf.

2.5.1. Wave event return period

Wave events return period was derived from coastal buoy time series to assess the intensity of hydro-meteorological events. The erroneous wave data were eliminated by the method of Butel et al. (2002). Cumulative probability distribution of the monthly maximum of H_{m0} (significant spectral wave height) and $T_{(0,2)}$ (mean spectral period) were computed to estimate the return period of wave events in a period from February 2006 to July 2020. The monthly maxima were extracted from the 30 min interval wave data. The Gumbel law is classically used to describe the probability distribution of extreme events (floods, rainfalls or waves). It was fitted to these data using the Maximum Likelihood method (Prescott and Walden, 1980). This analysis was done using MATLAB and the WAFO toolbox (Brodtkorb et al., 2000).

2.5.2. Suspended particulate matter properties

Suspended particulate matter (SPM) properties were inferred from coincident optical and acoustic backscatter measurements carried out by the glider. Depending on whether optical or acoustic methods are used, the scattering properties of sediment differ (Schulz et al., 2016).

Measured optical turbidity for a given concentration of suspended particles increases with decreasing particle size, due to both increased abundance and to light scattering from smaller particles. A spike analysis has been applied to characterize the presence of large particles, using the method described by Briggs et al. (2011). Spikes were recorded by all optical measurements as rapid transient, and often large increases in optical signals. A 5-point running minimum filter followed by a 5-point running maximum was applied on the raw optical backscattering profiles at 700 nm for the determination of the background (baseline) of each profile. Then, spike signal was calculated by subtracting the baseline from the raw optical profile.

Acoustical measurements were used to complete the description of coarse particles in the water column. Acoustic turbidity is determined by the ratio of energy received by the transducer (backscattered wave), over the emitted energy, corrected with the dispersion of the acoustic wave due to the adsorption of the seawater and the spherical spreading. The ADCP used in this work, with a frequency of 614 kHz, has a peak sensitivity for particles of 775 μm in diameter, which represents the upper limits of the observed aggregates in the GoL (Many et al., 2016). Furthermore, the ADCP samples large insonified volumes (until 1 m^3 at 20 m from the transducer), which may contain a significant number of aggregates.

Coincident optical and acoustic backscatter measurements show complementarity in the characterization of small and large suspended particles of the coastal area, respectively (Gentil et al., 2020).

2.5.3. The bottom boundary layer and surface-mixed layer

The bottom boundary layer (BBL) and surface mixed layer (SML) depths were estimated from the density profiles as the depth where the difference between the density and the reference value at 3 m above the seabed for the BBL, and below the surface for the SML was equal to 3×10^{-2} kg m^{-3} (Perlin et al., 2007). Based on density profile observations, this threshold density deviation has been preferred to 6×10^{-4} kg m^{-3}, used by Perlin et al. (2007) to assess the well-mixed BBL.

2.5.4. The rouse profile

Previous studies have clearly defined the standard Rouse profile for suspended sediment above the wave boundary layer in the unstratified layer (Glenn et al., 2008; Glenn and Grant, 1987; Miles et al., 2013; Styles and Glenn, 2000) as:

$$C_{(z)} = C_r \left[\frac{z}{z_r}\right]^{[-\gamma w f/\kappa u^*]} \quad (1)$$

where $C_{(z)}$ is the vertical concentration profile, C_r is the sediment con-

centration at the reference height z_r, γ is a constant ratio of eddy viscosities and diffusivities, κ is the von Karman's constant and u^x the friction velocity.

As in Glenn et al. (2008) and Miles et al. (2021, 2013), we use optical backscatter profiles averaged over 1.5 h, as a proxy for sediment concentration to study the sediment characteristics in the BBL. Profiles were normalized using the backscatter observed at a reference height of 4 m above the bottom, close to the bottom inflection point of the glider's sawtooth trajectory. The 4 m reference height ensures all profiles in each 1.5 h segment have data at this height and above. As prescribed by the Rouse profile, the relative backscatter profiles decay along a straight line in the BBL when plotted on this log-log scale. We fit a line linearly in log–log space to values of optical backscatter profiles in the BBL, in this case, constrained to the lower 5 m of the water column (Fig. 5). Profile fits where *r*-squared values were less than 0.8 were not included.

2.5.5. The bottom shear stress

The bottom shear stress (BSS) was estimated to assess the physical processes that drive the sediment resuspension. When dealing with currents only, the method to calculate the BSS (eq. (2)) consists in assuming a logarithmic velocity profile close to the bottom to characterize the friction velocity (eq. (3)).

$$\tau_c = \rho u_c^{x2} \tag{2}$$

$$u_c^x = \frac{\kappa u_{(z)}}{\ln(z/z_0)} \tag{3}$$

where, ρ is the density of water, u_c^x the friction velocity, κ the Von Karman constant (0.4), z the height of the measurement above the bottom, $u_{(z)}$ is the associated current velocity, and z_0 the bottom roughness.

Waves are also able to generate bottom shear stress (here noted τ_w) expressed from (eq. (4)).

$$\tau_w = 0.5\rho f_w {U_b}^2 \tag{4}$$

where U_b is the orbital velocity:

$$U_b = \frac{\pi H_s}{T\sin(kh)\sqrt{2}} \tag{5}$$

where H_s is the significant wave height, T the peak period, h the water depth, and k is the wavenumber corresponding to the peak period.

f_w is the wave friction factor expressed by (Swart, 1974):

$f_w = 0.3$ if $A/k_s < 1.57$

and beyond:

$$f_w = 0.00251\exp[5.21(A/k_s)^{-0.19}] \tag{6}$$

where A the orbital half excursion near the bottom:

$$A = \frac{U_b T}{2\pi} \tag{7}$$

and k_s the physical roughness related to the bottom roughness height through $z_0 = k_s/30$, in turbulent condition. A variety of models have been developed for predicting the non-linear combined wave- and current-induced BSS (Grant and Madsen, 1979; Holmedal et al., 2003; Shi and Wang, 2008; Soulsby et al., 1993). We used the Soulsby et al. (1993) formulation, widely used in the calculation of the BSS under the wave-current interaction (Jia et al., 2014). It allows estimating the wave-current shear stress (τ_{cw}) maximum within a wave period from the current alone shear stress (τ_c) and the wave alone shear stress (τ_w):

$$\tau_{cw} = \left[(\tau_m + \tau_w|\cos\varphi|)^2 + (\tau_w\sin\varphi)^2\right]^{0.5} \tag{8}$$

where (τ_m) is the shear stress averaged over the wave period which reflects the enhancement of turbulence by wave motions:

$$\tau_m = \tau_c\left(1 + 1.2\left[\frac{\tau_w}{\tau_w + \tau_c}\right]^{3.2}\right) \tag{9}$$

and φ is the angle between the wave propagation and the current. The wave-induced shear stress has been computed from WAVEWATCH-III simulations, since the wave orbital velocities cannot be determined by the glider. Therefore, the combined wave-current shear stress was estimated from the observation-model association.

2.5.6. The bottom roughness

The bottom roughness (z_0) is an important parameter for the prediction of sediment transport (resuspension and vertical diffusivity in the BBL) as well as for calculating the current profile near the sea bed. The bottom roughness depends on the physical roughness composed of three distinct elements (Nielsen, 1992): (1) the sediment grain size; (2) the morphology of the bed, including sedimentary bed structures such as ripples and morphological characteristics induced by benthic communities; and (3) the roughness associated with the near-bottom sediment transport. The resulting total physical roughness is assumed to be equivalent to the addition of the partial ones (Nielsen, 1992; Xu and Wright, 1995). Given the lack of information on the sediment properties (size distribution and bedforms) along the glider's path, it was decided to compute a range of bottom shear stress from an empirical range of bottom roughness based on two values. In cohesive muddy sand environments, a typical value found in the literature is 10^{-4} m (Ogston et al., 2008; Soulsby, 1997). This value was chosen as the low value of our physical roughness range. However, Fig. 2 shows the presence of biogenic material in abundance on the seabed of the outer shelf, such as indicated in Bassetti et al. (2006) with craters around 10 cm in diameter (see the two green points in Fig. 2b indicating a scale of 8 cm). For these reasons, a high value of 10^{-3} m was chosen, as found from observations where bedforms and biogenic material are observed (Cheng et al., 1999; Guillén et al., 2008; Peine et al., 2005).

2.5.7. SPM fluxes

Horizontal SPM fluxes are computed from current velocity and SPM concentration. SPM concentration was derived from a calibration (eq. (10)) carried out from the ship- and the same glider-based ECO-FLNTU instrument. The ship survey was carried out on the GoL (close to the study area) in winter (February 2015), which support the equivalent conditions assumption that our glider deployment (March 2018).

$$[SPM]_{OPT} = (1.27 \pm 0.45)xNTU + (1.05 \pm 0.85) \tag{10}$$

The integrated SPM fluxes were calculated throughout the water column, considering homogeneous currents and SPM concentrations in the portions of the surface and bottom layers not sampled by the glider. We estimated the uncertainty on SPM fluxes by propagating the average relative uncertainties related to the currents (0.06 m s^{-1}) from glider-ADCP data processing, and SPM concentrations (1 mg L^{-1}) from the calibration.

3. Results

3.1. Storm conditions

The hydro-sedimentary dynamics is studied along three periods from February 26 to March 4, 2018: (1) pre-storm, (2) storm, i.e., when the H_s >1.5 m, and (3) post-storm conditions, delimited in Fig. 3. Pre-storm conditions are characterized by a low-energy swell around 1 m high and a period of 4 s (Fig. 3b). At the beginning of the storm period (1st March), winds shift from north to southeast with moderate intensity (~15 m s^{-1}) (Fig. 3a). These southeast winds were related to a peak swell at the Sète buoy on 1 March (Fig. 3b) characterized by a significant wave height (H_s) of ~5.5 m, a maximum wave height (H_{max}) of 11 m, a period (T_s) around 10 s, and a direction of 100° (Fig. 3c). The wave

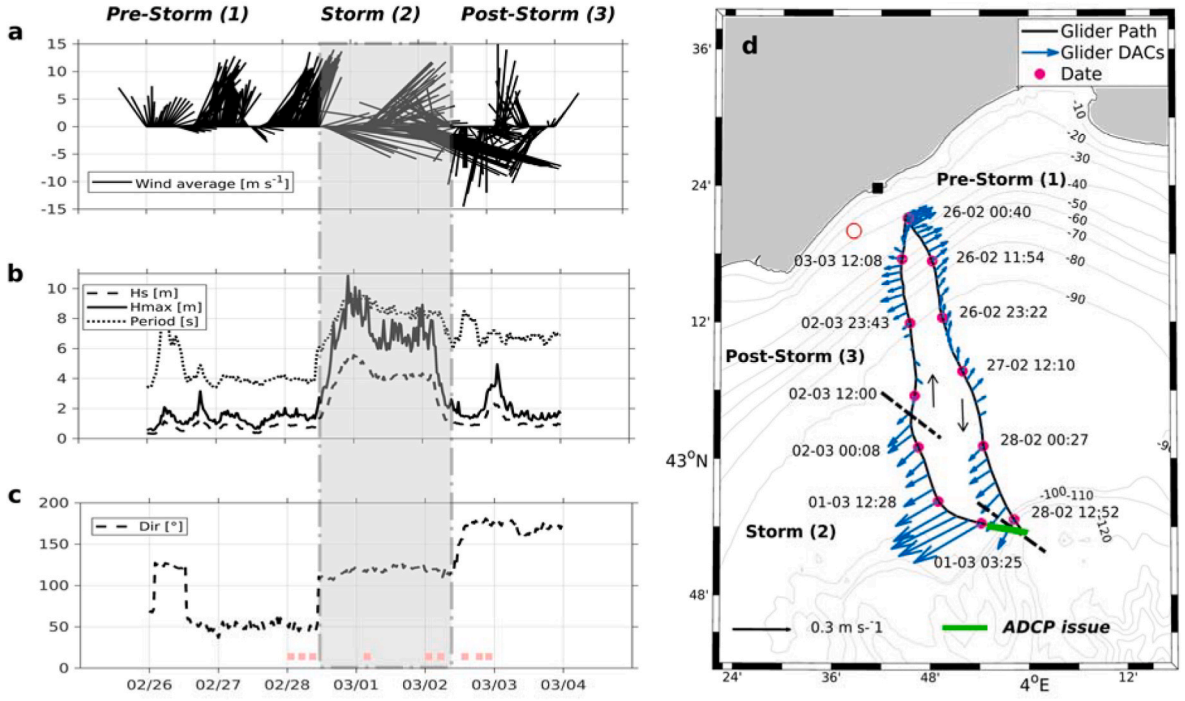

Fig. 3. (a) Wind speed and direction time series at the Météo-France Sète station (black square in Fig. 3d). By convention, wind direction indicates its origin. (b, c) Buoy time series (red circle in Fig. 3d) of significant wave height (Hs), maximum wave height (Hmax), wave period, and wave direction (Dir). The red squares, in panel c, indicate the time of the nine profiles displayed in Fig. 5. (d) Depth averaged current (blue arrows) superimposed on cross shelf glider tracks from 02/26 to 03/04 (black lines). The black arrows indicate the direction of the glider's motion. The temporal evolution of the meteorological conditions is indicated by periods 1,2,3 delimited by black dashed lines. The green line shows a gap in the glider data due to an issue from the ADCP sensor acquisition.

statistical analysis carried out over a period from 2006 to 2020 from the Sète buoy data showed a return period of 5.4 years for this event. In the post-storm period, the significant wave height dropped drastically. In total, the storm lasted 42 h. During the two sections studied, the Rhone River discharge was in average of 1900 $m^3 s^{-1}$, i.e., close to the mean annual flow of the river (1700 $m^3 s^{-1}$), stating that there is no significant discharge event.

The glider was deployed approximately 5 km offshore in the GoL and progressed perpendicular to the isobaths from the coast at ~30 m depth to the shelf edge at ~200 m depth (February 26–28 in pre-storm conditions), and back to the coast (March 1–4 in storm and post-storm conditions,see the black lines in Fig. 3d). Because storm currents are often faster than the typical maximum glider forward speed of about 0.3 m s^{-1}, passing storms can be readily identified in the glider track data as a deviation from the across shelf line. During the storm, the glider's deviation shows a south-westerly depth-averaged current on the outer shelf (Fig. 3d), which is a typical circulation under onshore winds in the GoL (Mikolajczak et al., 2020; Ulses et al., 2008a). However, Fig. 3d shows a gap in the glider data between 02/28 and 03/01 (green line) due to an ADCP sensor acquisition problem. This instrumental issue leads to missing the beginning of the storm, where the waves were the largest (Hs ~ 5 m on 03/01).

3.2. Cross-shelf glider sections

Fig. 4 shows a time series of hydrological, hydrodynamical, and biogeochemical properties of the water column for the three periods (pre-storm, storm, and post-storm).

During pre-storm conditions, a 2- to 3-layer system according to the temperature (Fig. 4d) and salinity (Fig. 4g) is observed. The interface between these layers is marked by an increase of the Brunt-Väisälä frequency, highlighting the stratification of the water column (Fig. 4j). Two cold (<10 °C) and low salinity (<37 g kg^{-1}) patches are observed at the surface at the two ends of the transect and correspond to the dispersion of the Rhone River plume over the GoL shelf. The seasonal pycnocline is marked by the isopycnal 28.9 kg m^{-3}, separating cold (<12 °C) and less salty (<38 g kg^{-1}) subsurface waters, from warmer and saltier bottom waters. Currents (Fig. 4b, e, h) show a weak depth-averaged intensity (<0.1 m s^{-1}) from the northeastern part over the mid shelf, turning into the southwestern part over the outer shelf (Fig. 3d). The vertical shear is low in the water column but increases close to the bottom where velocity decreases. Biogeochemical properties show subsurface waters rich in chlorophyll-a (~1.5–2 μ g L^{-1}) (Fig. 4l). In addition, an increase of optical backscatter (~1.5 NTU, Fig. 4c), shows the presence of a thin bottom nepheloid layer with a concentration of ~3 mg L^{-1}, and a subcritical Richardson number (<0.25), suggesting Kelvin-Helmholtz instabilities (Fig. 4k).

On 1st March during the storm period, the 28.9 kg m^{-3} isopycnal

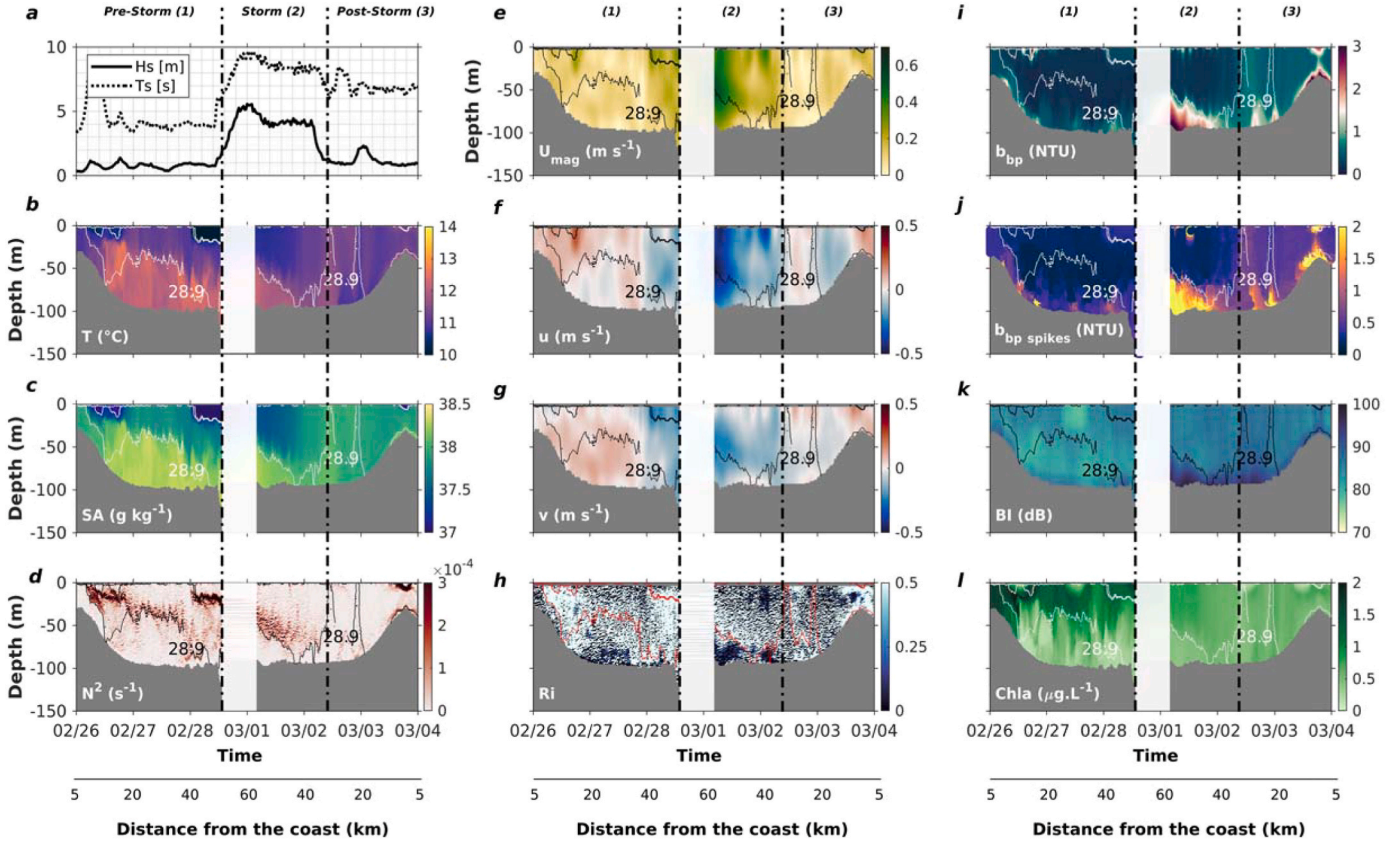

Fig. 4. Time series of (a) significant wave heights (Hs) and wave period (Ts), and glider time-series observations of hydrological ((b) temperature, (c) absolute salinity, (d) Brunt-Väisälä frequency), hydrodynamical ((e) current speed, (f) eastward velocities, (g) northward velocities, (h) Richardson number) and biogeochemical properties ((i) optical backscatter, (j) optical backscatter spikes, (k) acoustic backscatter index, (l) chlorophyll-a). The isopycnal 28.9 kg m^{-3} is superimposed on all plots and indicated by a solid black, white, or red line. Numbers 1–3 indicate three different storm regimes discussed in the text.

shifted in the water column from 80 to 55 m depth, switching to a two-layer system with homogenization of temperature and salinity in the subsurface and bottom waters (Fig. 4d, g). During this event, the currents have a maximum magnitude of around 0.5 m s^{-1} and are on average two to three times larger than pre-storm conditions and oriented southwest (Fig. 4b, e, h). In addition, the bottom nepheloid layer is up to 20 m thick, where Kelvin Helmholtz instabilities are still present and the concentration deduced from the optical backscatter is twice as high (6 mg L^{-1}) as under pre-storm conditions. An increase of the acoustic and optical spikes signal (Fig. 4f, i) is also observed and indicates the likely presence of large particles in the bottom nepheloid layer.

On 2 March at 12:00, the system transitioned toward a homogeneous water layer as the isopycnal 28.9 kg m^{-3} reaches the surface, with a temperature of ~11.5 °C, a salinity of ~38.3 g kg^{-1}, and currents falling at ~0.1 m s^{-1} throughout the water column. During this post-storm condition, the distribution of particles extends throughout the water column with higher values in optical and acoustic backscatter than during pre-storm conditions, while concentration in chlorophyll-a dropped by a factor three near the coast (~0.5 μ g L^{-1}).

3.3. Sediment dynamics

3.3.1. Vertical distribution of SPM and density in the water column

Fig. 5 shows three density anomaly and optical backscatter profiles for each of the three periods: pre-storm (a-c), storm (d-f), and post-storm conditions (g-i), represented in Fig. 3c by red squares. The dynamics of the BBL and SML are highly variable over time. From 1 March, where significant wave height and period increase, we observe a thickening of the bottom and surface mixed layers on profiles d to f (Blue and Red Squares, Fig. 5), related to a supercritical Richardson number (Fig. 4k) in the bottom boundary layer. A few hours after the end of the storm (Fig. 5g), the pycnocline appears to have been eroded via a complete mixing of the wind-driven surface layer and the bottom boundary layer.

The optical backscatter can be used to evaluate the characteristics of the suspended sediment in the water column. Profiles averaging, i.e., a 1.5 h average (~6 yos, between two surfacings) covers 1.5 km of the area based on the glider speed, providing a spatial description of the sediment characteristics. As describes by Glenn et al. (2008), it is a new way of looking at suspended sediment data that adds to other existing methods like tripods/ships. The time history of the normalized backscatter profiles (red stars, in Fig. 5) is clearly linked to the evolving density structure. As prescribed by the Rouse profile, the relative

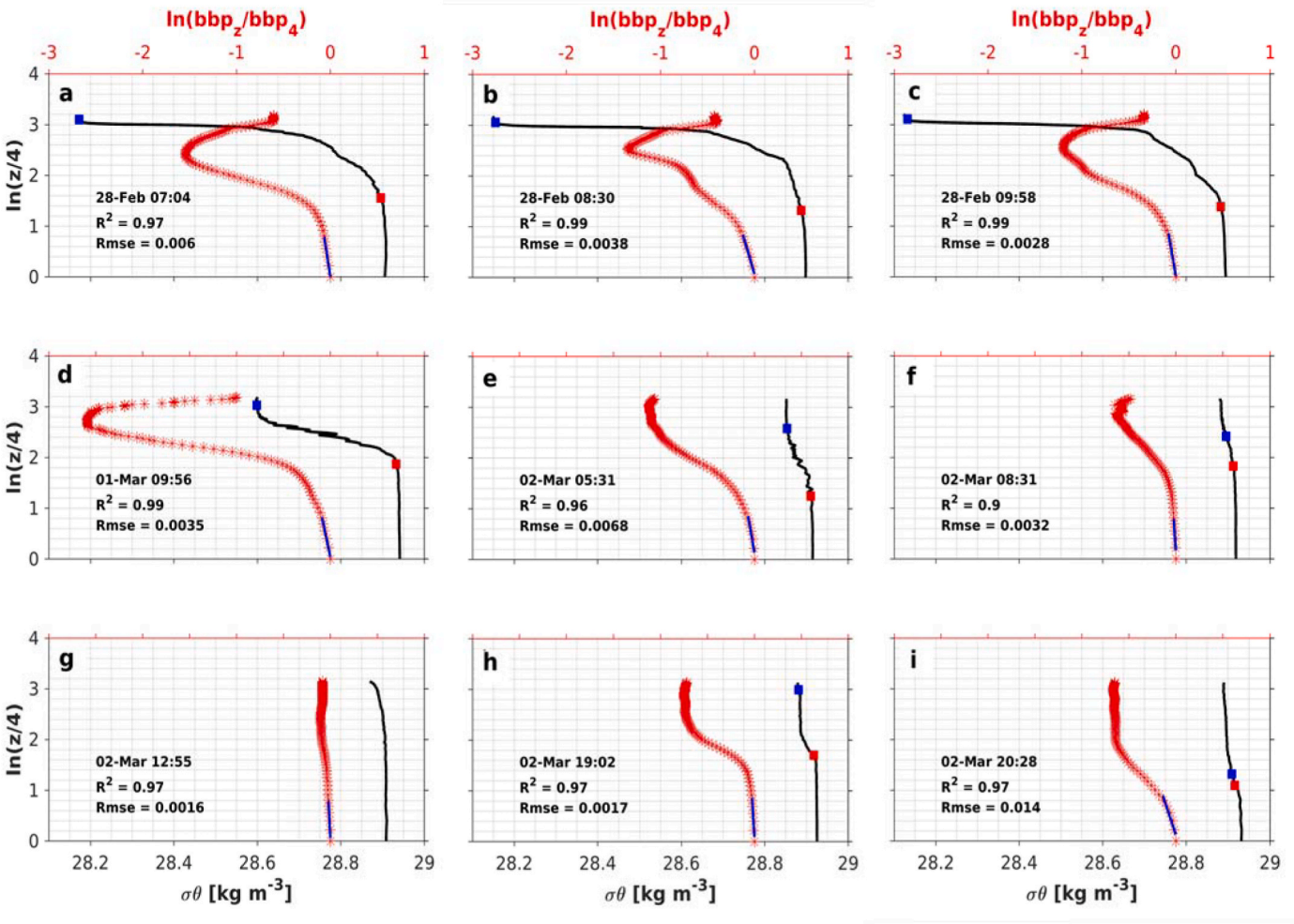

Fig. 5. X-axes are density profiles (black line, bottom scale) and logarithm of the normalized backscatter (top scale). Y-axis is the natural logarithm of depth divided by z_r. A straight line was fitted (blue line) to the normalized backscatter values below the bottom boundary layer whose thickness is indicated by a red square. The surface mixed-layer depth is also indicated (blue square).

backscatter profiles decay along a straight line when plotted on this log-log space until the bottom of the pycnocline is reached (Red Square, in Fig. 5). The highly significant correlations (p-value < 0.001), give us some confidence in the characterization of the Rouse profile in the BBL from optical backscatter profiles. When the pycnocline was eroded, the normalized backscatter profile is Rouse-like over the full water column, increasing vertical mixing of suspended sediment in the entire water column (Fig. 5g). As observed in Glenn et al. (2008) and Miles et al. (2013), the small amount of stratification caused by the temperature and salinity structure appears to be enough to inhibit the vertical turbulent flux of suspended sediment and significantly limit the amount of SPM reaching the upper water column (Fig. 5 a-f and 5h-i).

3.3.2. *Sediment fluxes*

During pre-storm conditions, current magnitude, SPM concentrations, and cumulative SPM fluxes in the BBL are weak, around 0.1 m s^{-1}, 2 mg $L^{-1,}$ and 4 mg m^{-2} s^{-1} respectively (Fig. 6 b-d). From 1 March the significant wave height increases rapidly (1–5 m, Fig. 6a), as do the currents (0.1–0.4 m s^{-1}, Fig. 6b), and SPM concentrations (2–5 mg L^{-1}, Fig. 6c) in the water column. Under these forcings, the thickness of the BBL increases to more than 20 m above the bottom as shown in Fig. 5d–f. During this period, cumulative SPM fluxes throughout the BBL reach up to 45 mg m^{-2} s^{-1} (Fig. 6d) oriented along the isobaths (Fig. 6e), approximately 10 times higher than during pre- and post-storm conditions. The maximum cumulative SPM fluxes in the water column are around 60 mg m^{-2} s^{-1}, estimated during the storm event (Fig. 6e). The majority of the sediment fluxes are in the bottom layer since they represent 75% of the total SPM fluxes in the water column. After the storm, the average SPM concentration remains relatively high (~3.5 mg L^{-1}, about twice the pre-storm concentrations) in the entire water column, and persists more than 40 h after the end of the storm.

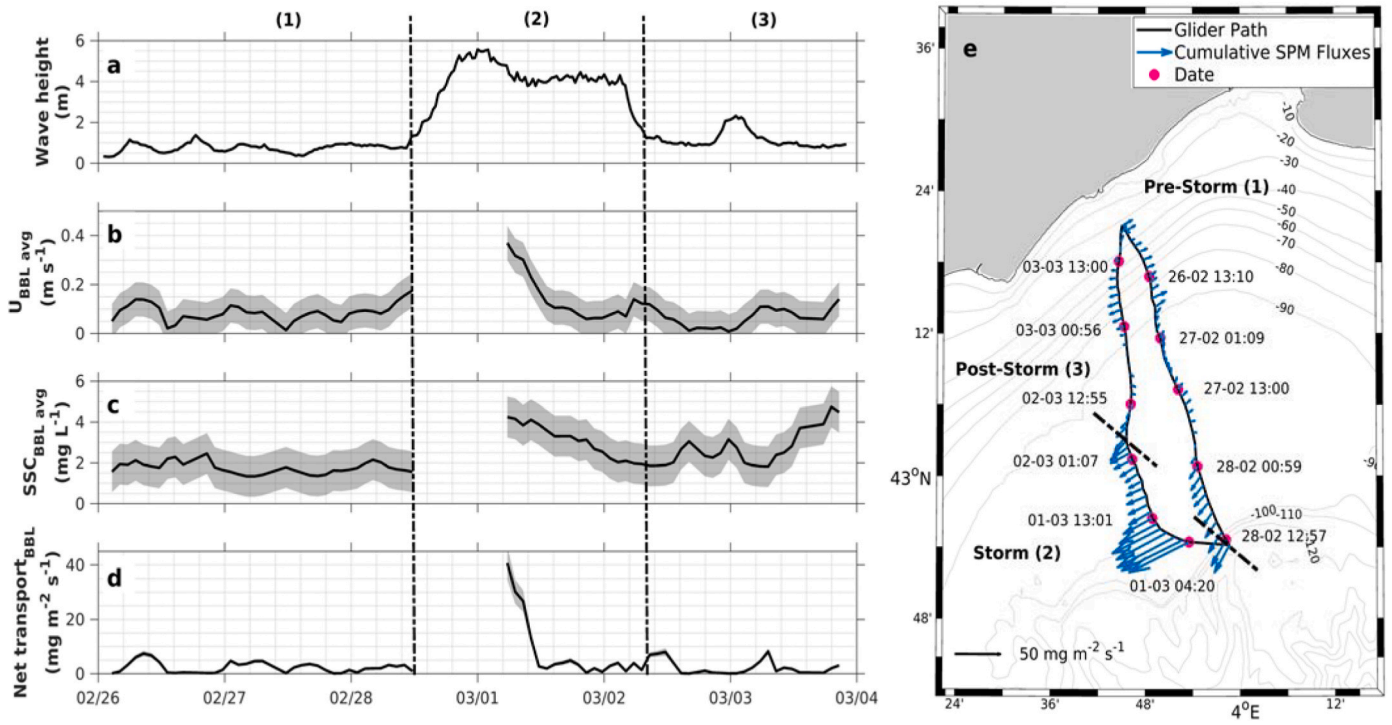

Fig. 6. Time series of (a) significant wave height, and hydro-sedimentary parameters in the bottom boundary layer: (b) depth-averaged currents, (c) SPM average concentration, (d) vertical cumulative SPM fluxes. The shaded grey area is the average uncertainty. (e) Map of vertical cumulative SPM fluxes (blue arrows) and cross-shelf glider tracks (black lines) from February 26 to March 04. The pre-, peak-, and post-storm periods are delimited by black dashed lines.

3.4. Model validation

To validate the wave and current simulations, we calculated correlation coefficients and root-mean-square-error between modeled and observed significant waves height at the coastal buoy and depth averaged currents along the glider track.

Simulated wave heights (Fig. 7b) are underestimated during the peak of the storm (around 00.00 h on 1 March), up to 1.2 m difference from

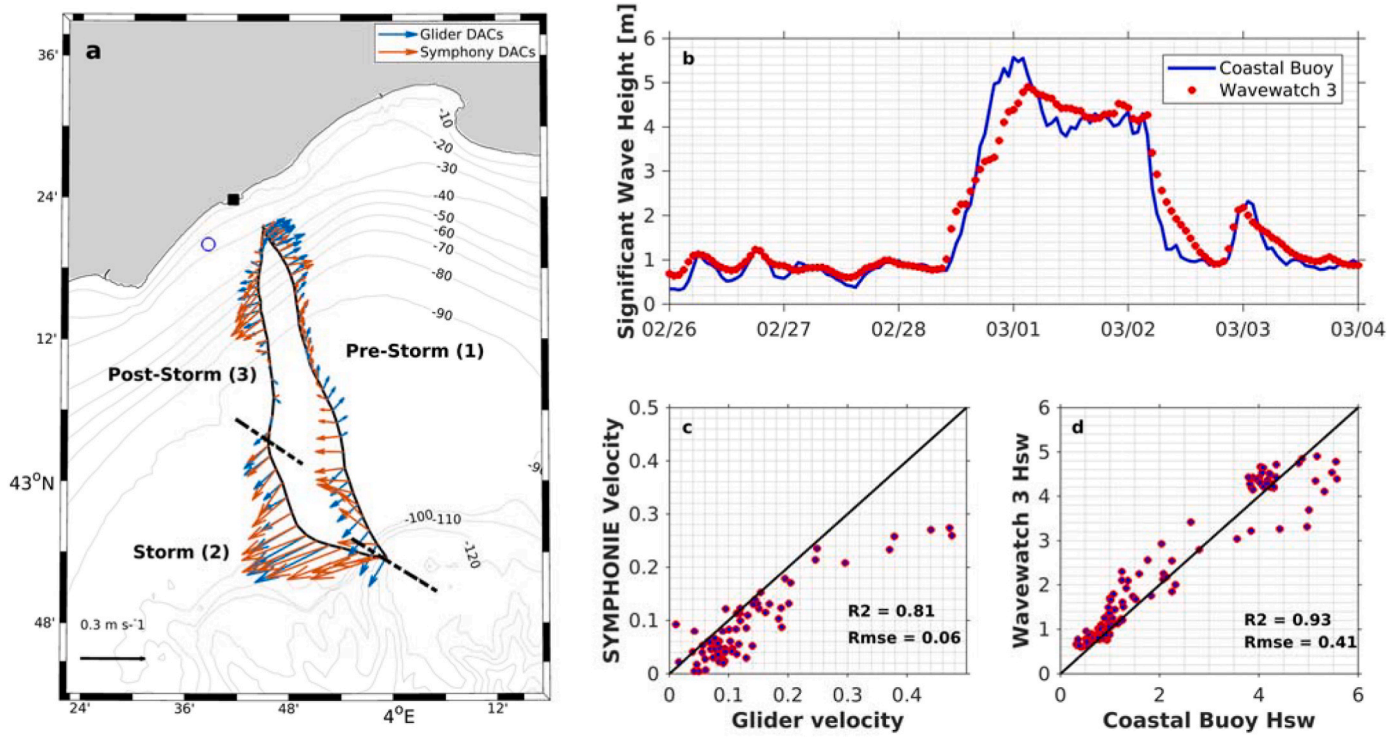

Fig. 7. (a) Depth-averaged currents simulated with SYMPHONIE (orange arrows) and deduced from the glider dead reckoning (blue arrow). The location of the coastal buoy is represented by the blue circle, while the pre-, peak-, and post-storm periods are delimited by black dashed lines. (b) Significant wave heights measured at the buoy (blue) and simulated with WAVEWATCH-III at the same point (red). (c, d) Correlations and RMSE between modeled and observed depth-averaged currents and significant wave heights, respectively.

the observed values. Outside this peak, during the high wave event (~4.5 m) and the pre- and post-storm periods, the simulation is in line with observations, as confirmed by a highly significant correlation (p-value <0.001, $r^2 = 0.93$), and a RMSE of 0.41 m (Fig. 7d). In addition, we compared the average waves direction measured (coastal buoy) and simulated (WW3) during the storm. The results are very close, since the mean waves direction is 122° and 130° for measurement and simulation, respectively.

To assess modeled currents, we compared the hourly mean depth-averaged values extracted from the nearest grid point to each glider surfacing, to depth and time-averaged glider currents using dead reckoning (see section 2.1.3 Glider data processing). The SYMPHONIE simulated currents are in good agreement in intensity and direction with the observed glider currents for the majority of the deployment (Fig. 7a) with the area of minimum current in the middle of the glider path and the reversal of the current between the pre- and post-storm periods in the vicinity of the inner shelf. The coefficient of determination (r^2) between measured and modeled currents is 0.81, with a RMSE of 0.06 m s^{-1} (Fig. 7c), which is a value identical to the uncertainty of the absolute velocity estimated from the glider-ADCP.

3.5. Physical processes driving resuspension

3.5.1. Along the glider path

Fig. 8 shows the time series of the bottom shear stress generated by waves and currents and their combined impact as a function of the distance to the coast. The current-induced bottom shear stress was calculated from the glider data and by the SYMPHONIE model collocated in time and space with the glider. The wave-induced shear stress was calculated from WAVEWATCH-III results rather than the series measured at the buoy to account for (i) wave inhomogeneity along the glider path, and (ii) wave attenuation during storm conditions in shallow waters of the buoy site. Finally, the combined wave-current shear stress was estimated from the observation-model association. As mentioned before, given the limited information on the surface sediment along the glider path, we chose to perform a sensitivity analysis to the bottom roughness with values of 10^{-4} m (blue line) and 10^{-3} m (red line).

During pre-storm conditions, the glider sails offshore on a bottom depth ranging from 30 to 95 m. Over this period, currents and waves are too weak to generate bottom shear stress larger than 0.03 N m^{-2} whatever the bottom roughness value used. From 1 March, when the marine storm impacts the shelf, the glider is over the outer shelf (>90 m). The highest values recorded at the offshore end of the transect range between 0.1 and 0.25 N m^{-2} for the current-induced bottom stress depending on whether we consider the model or the glider and depending on the two values of the roughness (Fig. 8a). The highest values of modeled wave-induced shear stress were between 0.1 and 0.45 N m^{-2} (Fig. 8b). Whatever the value of bottom roughness, Fig. 8 shows that currents, waves, or the interaction of these two forcings are likely to resuspend sediment. Indeed, critical shear stress for muddy sands of the outer shelf range from 0.03 to 0.11 N m^{-2} (grey band, Fig. 8) (Ahmad et al., 2011; Soulsby, 1983). On the outer-shelf, during the swell peak, the sensitivity analysis shows that for a bottom roughness of 10^{-4} m, the

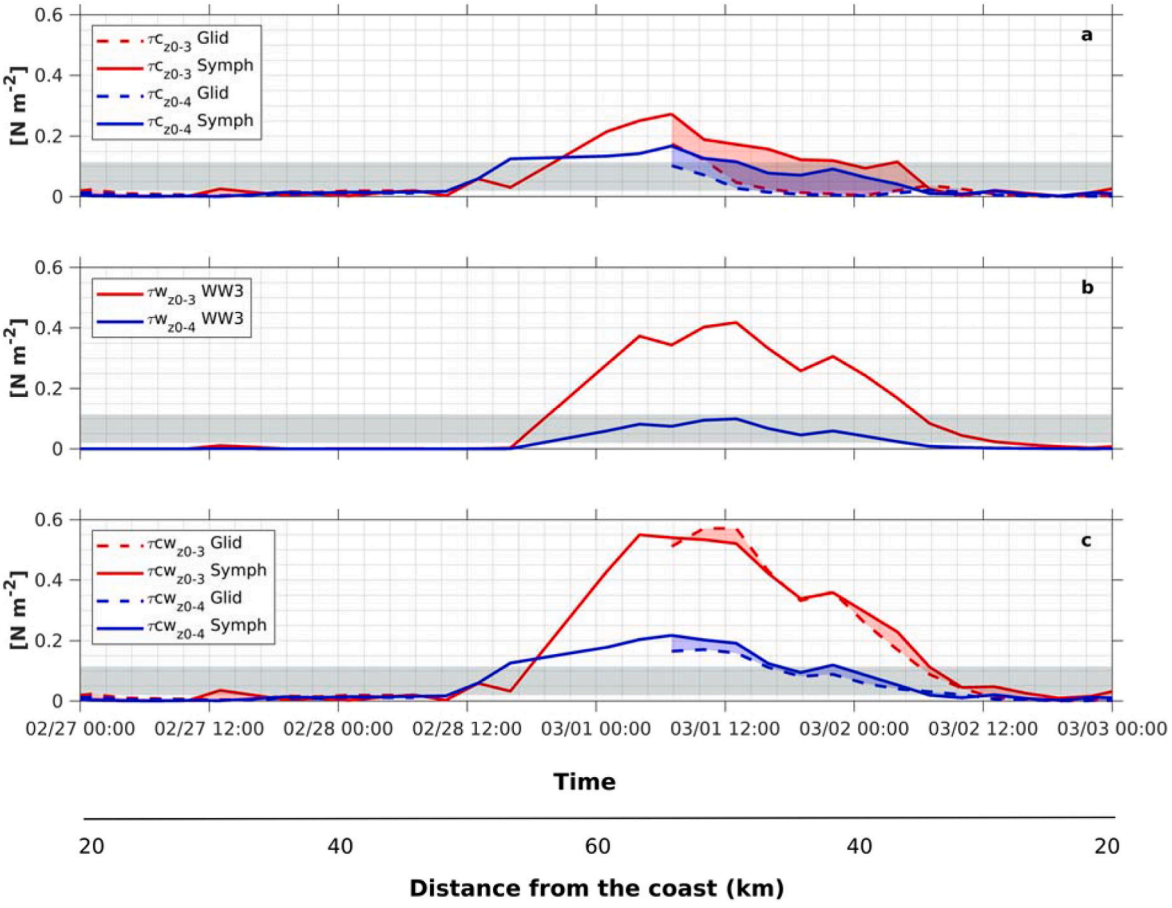

Fig. 8. Comparisons of bottom shear stress (BSS) derived from the glider (dashed lines) and SYMPHONIE/ WAVEWATCH-III models (solid lines) for (a) currents, (b) waves (no glider), and (c) wave-current interactions along the glider path with two values of the bottom roughness, 10^{-4} m (blue) and 10^{-3} m (red). Typical resuspension critical shear stress for the muddy sands of the GoL is indicated by the grey band. Note that the glider does not produce any observations at the beginning of the storm between 28 February 11 a.m. and 01 March 5 a.m.

wave and current stresses are of the same magnitude (~0.15 N m^{-2}), while the wave stress can be up to 2 times the current stress (~0.45 and 0.22 N m^{-2}, respectively), for a bottom roughness of 10^{-3} m, making it the main contributor to total bottom shear stress (τ_{cw} in Fig. 8c).

The model overestimates the current-induced bottom stress compared to the glider (Fig. 8a) due to a current in the BBL stronger than in the observations despite similar depth-averaged currents. However, this overestimation has a limited impact on the total shear stress (Fig. 8c), since waves are the major contributor to the total stress during the storm (Fig. 8b). We have seen that the modeled waves are well represented in significant heights and directions when compared to the Sète buoy (see section 3.4). The convincing comparison between observed and simulated waves and currents gives confidence in extrapolating results across the entire shelf during the storm event from the numerical simulation.

3.5.2. *Overall spatial variability*

Maps of the wave-current BSS averaged from 0:00 a.m. to 03:00 h on 1 March, during the storm, calculated for both values of the bottom roughness are plotted in Fig. 9a and b. The depth-averaged currents superimposed on the figures are westward and along isobaths on the shelf, which is a classical circulation during marine storms in the GoL. The entire GoL was affected by the storm, but the currents in the central part of the shelf explored by the glider were weaker than those to the west and east, where the narrower shelf accelerated the flow. The significant wave height averaged over the same period as the bottom stress is shown in Fig. 9c. In shallow water, BSS is larger due to a greater interaction between the bottom and the swell. Comparison of the BSS distribution with representative surface granulometric sediment distribution data (not shown here) shows that resuspension may occur during this storm over the outer shelf (isobaths>90 m). Indeed, minimum values of 0.1 and 0.3 N m^{-2} are observed on the 100 m isobath (Fig. 9 a-b), with the 10^{-4} and 10^{-3} m z_0 simulation, respectively. These values are close to the resuspension critical shear stress assessed for muddy sands as discussed above.

4. Discussion

Acoustic and optical data sets from winter glider transects have shown, outside of storm periods, the existence of a 2- or 3-layer vertical stratification characterized by the presence of a low salinity water layer from the Rhone River. This upper layer, in the first tens of meters, is cooled by air-sea fluxes, while the bottom layer is characterized by the presence of more salty offshore water. This stratification produces a decoupling of currents accelerated in the surface layer by the wind, and also of passive tracers such as chlorophyll-a largely concentrated in the surface layer or suspended matter in the bottom layer. The arrival of an offshore storm (5 years of return period) associated with a strong swell leads to an increase in SPM in the near-bottom outer-shelf as shown by glider observations. The storm unstratifies the water column up to 90 m depth via a complete mixing of the wind-driven surface layer and the bottom boundary layer. The vertical mixing is then sufficiently strong to allow the diffusion of the suspended matter over the entire water column. Similar observations were recorded on the meso-tidal Mid-Atlantic Bright shelf (Glenn et al., 2008; Miles et al., 2013). Modeling suggests that the bed shear stress may be able to resuspend sediment on the outer-shelf. In addition, the glider-ADCP platform highlighted along-shelf SPM fluxes during the storm (Fig. 6d), suggesting advection of particles from east to west in on GoL's shelf. The increase in SPM in the water column is likely due to the combination of resuspension and advection processes on the shelf. However, the glider performs the open-coast section over 3 days, i.e., about 4 periods of inertial oscillation (~17.5 h) in the GoL. The variability of currents on scales smaller than the transit time along the transect, generally does not allow assuming a steady state. This non-simultaneity of the measurements along the transect represents the main limitation of the contribution of the glider

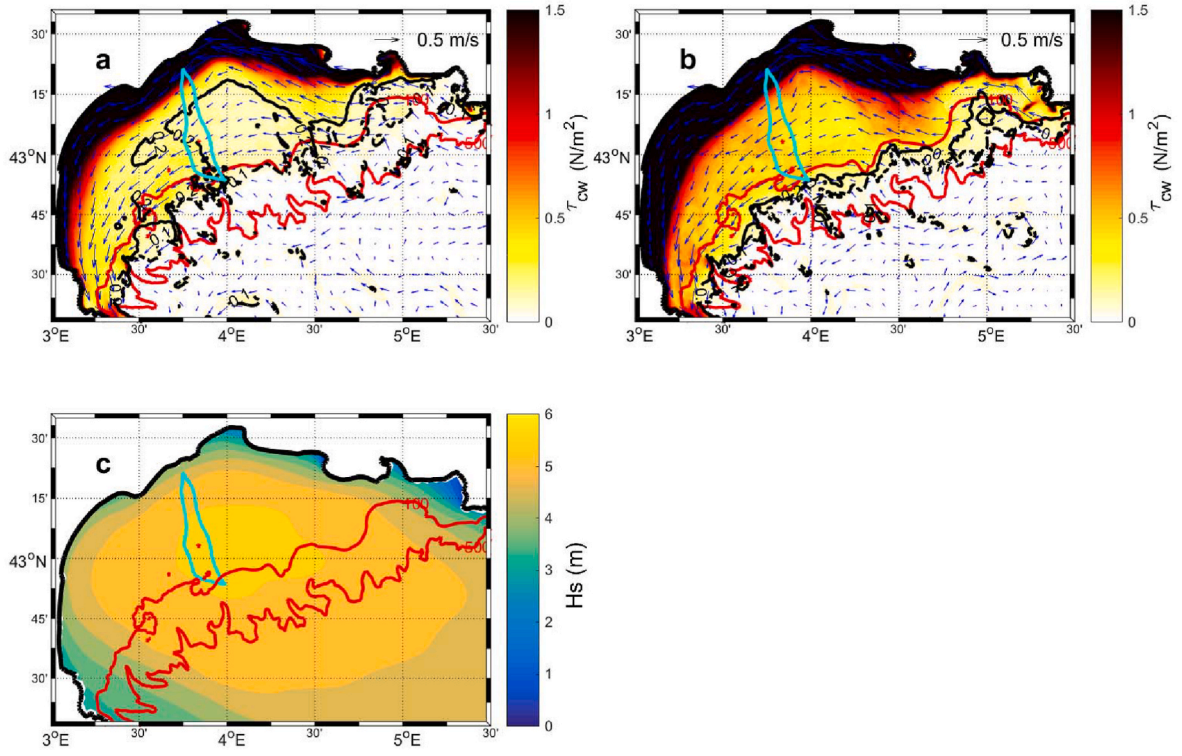

Fig. 9. (a) and (b) background color: wave-current bottom shear stress (N m^{-2}) averaged between 00:00 and 03:00 h on March 1, 2018 from the simulations using a roughness of 10^{-4} (a) and 10^{-3} m (b). Note that the colorbar has been saturated on the inner shelf to focus on the deeper areas. The black lines correspond to the 0.2 (solid line) and 0.1 (dashed line) N m^{-2} isolines. The depth-averaged currents are superimposed. (c) Significant wave height (m) calculated by WAVEWATCH-III averaged over the same period. For the three maps, the red lines correspond to the 100 m and 500 m isobaths, and the cyan line corresponds to the glider path.

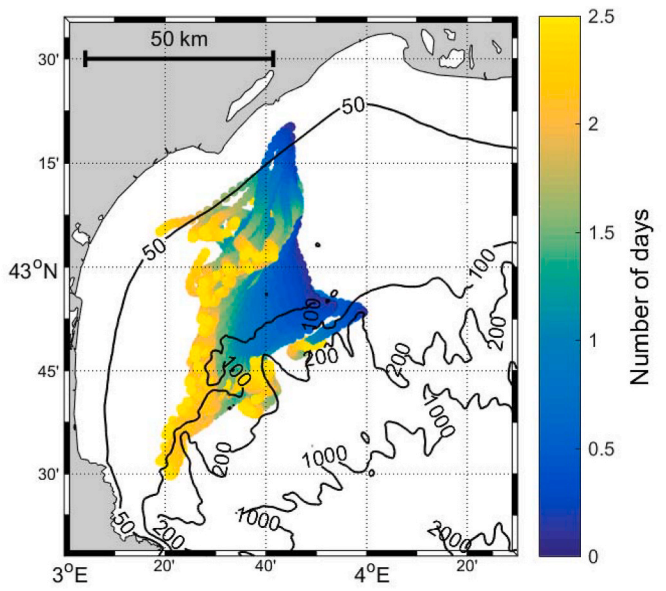

Fig. 10. 2.5-days transport of Lagrangian particles representing fine particles in suspension initially present along the "storm" glider section. The particles are released on 28 February 17:00 during the ascending phase of the storm (see Fig. 7b).

to the study of transport at regional scale. On the other hand, if it is used in conjunction with fixed moorings and/or in connection with the modeling, its contribution is indisputable as shown hereafter.

The importance of currents and surface waves was examined in the bottom boundary layer during the storm, to assess mechanisms driving the sediment resuspension on the muddy sands of the outer shelf. The glider-ADCP provides valuable near-bed data to describe the sediment dynamics, but the resolution used was not sufficient to derive the bottom roughness, a key parameter for quantifying bottom shear stress. We have therefore set a range of values based on the available particle size samples, seabed images close to the glider path, and typical values used in the literature for muddy sands with biological contents (Guillén et al., 2008; Ogston et al., 2008; Peine et al., 2005; Soulsby, 1997). From these assumptions, and thanks to the convincing comparison between observed and simulated waves and currents, (see section 3.4), we used numerical simulations to estimate BSS along the glider pathway. Simulation showed that current, wave, and their interactions may induce stress able to remobilize sediments from the seabed. Estimations of BSS highlight that wave-induced stress (0.15–0.45 N m $^{-2}$) can be up two times greater than the current-induced stress (0.15–0.22 N m $^{-2}$) in the selected bottom roughness ranges (10^{-4} to 10^{-3} m). Therefore, modeling suggests that waves stress would be primarily responsible for sediment resuspension on the outer-shelf of the GoL during a 5-years return period storm. These results are coherent with recent observations carried out in the Valencia shelf, NW Mediterranean (Simarro et al., 2015), where waves have been identified as the main driver of sediment resuspension and in the Monterey Bay, California (Rosenberger et al., 2016), where waves are an essential forcing of the sediment resuspension in addition to internal tides currents. In addition, the modeled wave-current-induced stress, during the peak of the storm, shows conditions conducive to sediment resuspension over the whole shelf (inner-, mid-, and outer-shelf, Fig. 9a and b). Bottom shear stress intensity may could enough to remobilize the uppermost muddy sediment layer that blankets the outer shelf, and up to the relict coarser sands (~150 μm) found beneath the surface layer for bottom roughness of 10^{-4} and 10^{-3} m, respectively.

Previous studies have highlighted alongshore transport as the dominant feature of storm-driven sediment transport on continental shelves (Miles et al., 2013, 2015; Ogston and Sternberg, 1999; Styles and Glenn, 2005). This alongshore transport induced by marine storms also exists in the GoL (Bourrin et al., 2015; Guillén et al., 2006; Palanques et al., 2008, 2006; Ulses et al., 2008a). The model results allow characterizing the advection of the suspended particles during the storm from the spatiotemporal variability of currents. Strong westward currents (~0.4 m s^{-1}) persist during 2.5-days from the 28 February 17:00, associated with a sustained increase in turbidity in the water column as shown by the glider observations (Fig. 4). These observations emphasize the necessity to monitor the outer shelf to improve our understanding of SPM dynamics at the shelf scale. To evaluate the displacement of suspended matter at the regional scale, Lagrangian particles were positioned in the model current fields along the "storm" transect of the glider and throughout the water column. The particles were released at the beginning of the storm every 10 m, from 20 m below the surface to the bottom. Deposition was neglected to simulate the particles that remain in suspension throughout this period. Fig. 10 shows the trajectories of the particles, all points combined. The 2.5-days storm associated with currents of ~0.4 m s^{-1}, produces a displacement of SPM of ~68 km to the southwest, with a rapid transport from the beginning of the storm at 90–100 m depth, since the particles are displaced nearly 37 km on the 1st day. The storm duration is not sufficient for the suspended material in the central part of the shelf (study area) to be exported from the GoL. However, it is likely that this matter will be exported during the next storm, even if it is moderate. Indeed, the muddy sediment deposits in the southwestern part of the GoL are easily remobilized (compared to the mid-shelf) due to the narrowing of the shelf producing a strengthening of the storm-induced bottom currents (DeGeest et al., 2008). Finally we can infer that sediment could be transferred from the proximal zone of the Rhone to the southwestern outlet of the GoL in a discontinuous manner, with a jump of a few tens of kilometers at each storm. Annual storms are probably sufficient to produce these jumps up to 60 m depth along the mid-shelf mud belt, where most of the along-shelf transport is probably concentrated. Concerning the outer-shelf, a hypothesis would be a seeding in suspended matter to the south/south-west of the Rhone by the plume which extends towards the open sea in the dominant conditions of northern wind (Estournel et al., 1997). Although the extremity of the plume is lightly loaded with suspended matter, the frequency of river borne plumes could indicate the source of the deposits that drape the outer shelf sands. Following this initial deposition, southwestward transport would occur during the most energetic storms. Furthermore, Ekman transport in the bottom nepheloid layer, induced by the general cyclonic circulation of the GoL, could also contribute to the transport of fine sediments from the shelf to the open sea, feeding the outer shelf (Durrieu de Madron and Panouse, 1996). Finally, this alongshelf transfer model proceeding by successive jumps, involves temporary deposits, consistent with Miralles et al. (2005) observations, showing that sedimentation rates in the central part of the GoL are around 0.1 cm year^{-1} at scales of several decades. This study improves knowledge of the fate of the muddy sands over the outer shelf of the GoL—also found on many continental margins into the world.

5. Conclusion

In this study, a Teledyne-Webb Slocum glider successfully sampled the outer-shelf of the Gulf of Lions during a 5-year return period storm. The active acoustic glider measurements proved invaluable validation of current vertical profiles of the hydrodynamic model, while observations of this type of event are generally lacking in the coastal continuum due to their rarity. Numerical simulation suggests sediment resuspension at the shelf scale during the storm event, associated with an along-shelf transport reaching 70 km for the fine fraction of the outer shelf. These results show that several storms are needed to export the fine fraction of suspended materials of the central part of the Gulf of Lions' shelf towards the open-ocean. This study highlights the complementarity between numerical modeling and new technology observations such as gliders, designed to spatially extend the measurement of sediment

characteristics. This approach allowed us to draw new insights on the fate of the muddy-sands over the outer shelf of the Gulf of Lions—also found on many continental margins into the world—especially during sporadic events, which are the main drivers of sediment dynamics. The recent integration of a Laser In Situ Scattering and Transmissometry (LISST) sensor into glider should allow observing of the details of suspended particle size and concentration, opening up new perspectives in understanding particle aggregation and settling processes at regional scales. Improved in situ observations of particle properties will be valuable for the validation of sediment resuspension and transport model to assess the impact of episodic events in the coastal zones.

Funding

The corresponding author is funded through a PhD grant of French Occitanie Region. This work was funded by the EC2CO CHIFRE (AO-2018), the MATUGLI (ANR 14-ASTR-0021-01), and the MELANGE (ANR-19-ASMA-0004) projects.

Declaration of competing interest

The authors declare that they have no known competing financial interests or personal relationships that could have appeared to influence the work reported in this paper.

Acknowledgements

We thank the Parc National des Gliders of the DT INSU, for the integration of the ADCP, glider deployment, and piloting. We thank Yann Leredde of the University of Montpellier, leader of the CHIFRE project and all the contributors. We also thank reviewer Kurt Rosenberger, an anonymous reviewer, and the journal editor for their constructive and thoughtful comments and suggestions.

References

Agence des aires marines protégées, COMEX, GIS Posidonie, Equipe scientifique — MEDSEACAN 2008-2012, 2012. Programme de reconnaissance des têtes de canyons de la Méditerranée française.

Augris, C., Agin, G., Berne, S., Arnaud, M., Guizien, K., Chatelain, M., Labrune, C., Carbonnel, P., Maillet, G., Grenz, C., Vella, C., Nittrouer, C.C., Bourrin, F., Certain, R., Durrieu De Madron, X., Garlan, T., Dufois, F., Jouet, G., Dennielou, B., Simplet, L., 2013. Seabed substrate database from a compilation of sediment samples taken during oceanographic campaigns carried out in the Gulf of Lion by Ifremer, CEFREM, IRSN, CEREGE, FOB, MIO, LECOB, The Conseil Général de l'Hérault and Rhône-Méditerranée-Corse Water Agency. Results of grain size analysis performed on samples. SEANOE. https://doi.org/10.17882/81430.

Ahmad, M., Dong, P., Mamat, M., Wan Nik, W., Mohd, M., 2011. The critical shear stresses for sand and mud mixture. Appl. Math. Sci. 5, 53–71.

Aloısi, J., 1986. Sur un modele de sédimentation deltaıque : contribution a la connaissance des marges passives. These de Doctorat d'Etat, Université de Perpignan.

Bassetti, M.-A., Jouet, G., Dufois, F., Berné, S., Rabineau, M., Taviani, M., 2006. Sand bodies at the shelf edge in the Gulf of Lions (Western Mediterranean): deglacial history and modern processes. Mar. Geol. 234, 93–109.

Berne, S., Lericolais, G., Marsset, T., Bourillet, J.F., De Batist, M., 1998. Erosional offshore sand ridges and lowstand shorefaces; examples from tide-and wave-dominated environments of France. J. Sediment. Res. 68, 540–555.

Bonnin, J., Heussner, S., Calafat, A., Fabres, J., Palanques, A., De Madron, X.D., Canals, M., Puig, P., Avril, J., Delsaut, N., 2008. Comparison of horizontal and downward particle fluxes across canyons of the Gulf of Lions (NW Mediterranean): meteorological and hydrodynamical forcing. Continent. Shelf Res. 28, 1957–1970.

Bourcart, J., 1945. Etude des sédiments pliocènes et quaternaries du Roussillon: service Carte Géologique de France. Bulletin 45, 395–476.

Bourrin, F., Friend, P.L., Amos, C.L., Manca, E., Ulses, C., Palanques, A., De Madron, X.D., Thompson, C.E., 2008. Sediment dispersal from a typical mediterranean flood: the têt river, Gulf of Lions. Continent. Shelf Res. 28, 1895–1910.

Bourrin, F., Many, G., De Madron, X.D., Martín, J., Puig, P., Houpert, L., Testor, P., Kunesch, S., Mahiouz, K., Béguery, L., 2015. Glider monitoring of shelf suspended particle dynamics and transport during storm and flooding conditions. Continent. Shelf Res. 109, 135–149.

Briggs, N., Perry, M.J., Cetinić, I., Lee, C., D'Asaro, E., Gray, A.M., Rehm, E., 2011. High-resolution observations of aggregate flux during a sub-polar North Atlantic spring bloom. Deep Sea Res. Oceanogr. Res. Pap. 58, 1031–1039.

Brodtkorb, P.A., Johannesson, P., Lindgren, G., Rychlik, I., Ryden, J., Sjö, E., 2000. WAFO-a Matlab toolbox for analysis of random waves and loads. In: Presented at the the Tenth International Offshore and Polar Engineering Conference. International Society of Offshore and Polar Engineers.

Butel, R., Dupuis, H., Bonneton, P., 2002. Spatial variability of wave conditions on the French Atlantic coast using in-situ data. J. Coast Res. 96–108.

Chang, G., Dickey, T., Williams III, A., 2001. Sediment resuspension over a continental shelf during hurricanes edouard and hortense. J. Geophys. Res.: Oceans 106, 9517–9531.

Cheng, R.T., Ling, C., Gartner, J.W., Wang, P., 1999. Estimates of bottom roughness length and bottom shear stress in South San Francisco Bay, California. J. Geophys. Res.: Oceans 104, 7715–7728.

Dalyander, P.S., Butman, B., Sherwood, C.R., Signell, R.P., Wilkin, J.L., 2013. Characterizing wave-and current-induced bottom shear stress: US middle Atlantic continental shelf. Continent. Shelf Res. 52, 73–86.

Davis, R.E., Eriksen, C.C., Jones, C.P., 2002. Autonomous buoyancy-driven underwater gliders. technol appl auton underwater vehicles 37–58.

de Fommervault, O., Besson, F., Beguery, L., Le Page, Y., Lattes, P., 2019. SeaExplorer underwater glider: a new tool to measure depth-resolved water currents profiles. In: Presented at the OCEANS 2019-Marseille. IEEE, pp. 1–6.

DeGeest, A., Mullenbach, B., Puig, P., Nittrouer, C., Drexler, T.M., de Madron, X.D., Orange, D., 2008. Sediment accumulation in the western Gulf of Lions, France: the role of Cap de Creus canyon in linking shelf and slope sediment dispersal systems. Continent. Shelf Res. 28, 2031–2047.

Deines, K.L., 1999. Backscatter estimation using broadband acoustic Doppler current profilers. In: Presented at the Proceedings of the IEEE Sixth Working Conference on Current Measurement (Cat. No. 99CH36331). IEEE, pp. 249–253.

Drake, D.E., Cacchione, D.A., 1986. Field observations of bed shear stress and sediment resuspension on continental shelves, Alaska and California. Continent. Shelf Res. 6, 415–429.

Drake, D.E., Cacchione, D.A., Grant, W.D., 1992. Shear stress and bed roughness estimates for combined wave and current flows over a rippled bed. J. Geophys. Res.: Oceans 97, 2319–2326.

Dufois, F., Garreau, P., Le Hir, P., Forget, P., 2008. Wave-and current-induced bottom shear stress distribution in the Gulf of Lions. Continent. Shelf Res. 28, 1920–1934.

Durrieu de Madron, X., Panouse, M., 1996. Transport de matière particulaire en suspension sur le plateau continental du Golfe du Lion. Situation estivale et hivernale. In: Comptes rendus de l'Académie des sciences. Série 2. Sciences de la terre et des planètes, 322, pp. 1061–1070.

Durrieu de Madron, X., Wiberg, P.L., Puig, P., 2008. Sediment Dynamics in the Gulf of Lions: the Impact of Extreme Events.

Emery, K., 1968. Relict sediments on continental shelves of world. AAPG (Am. Assoc. Pet. Geol.) Bull. 52, 445–464.

Eriksen, C.C., Osse, T.J., Light, R.D., Wen, T., Lehman, T.W., Sabin, P.L., Ballard, J.W., Chiodi, A.M., 2001. Seaglider: a long-range autonomous underwater vehicle for oceanographic research. IEEE J. Ocean. Eng. 26, 424–436.

Estournel, C., Durrieu de Madron, X., Marsaleix, P., Auclair, F., Julliand, C., Vehil, R., 2003. Observation and modeling of the winter coastal oceanic circulation in the Gulf of Lion under wind conditions influenced by the continental orography (FETCH experiment). J. Geophys. Res.: Oceans 108.

Estournel, C., Kondrachoff, V., Marsaleix, P., Vehil, R., 1997. The plume of the Rhone: numerical simulation and remote sensing. Continent. Shelf Res. 17, 899–924.

Estournel, C., Marsaleix, P., Ulses, C., 2021. A new assessment of the circulation of atlantic and intermediate waters in the eastern mediterranean. Prog. Oceanogr. 198, 102673.

Ferré, B., Durrieu De Madron, X., Estournel, C., Ulses, C., Le Corre, G., 2008. Impact of natural (waves and currents) and anthropogenic (trawl) resuspension on the export of particulate matter to the open ocean: application to the Gulf of Lion (NW Mediterranean). Continent. Shelf Res. 28, 2071–2091.

Ferré, B., Guizien, K., De Madron, X.D., Palanques, A., Guillén, J., Grémare, A., 2005. Fine-grained sediment dynamics during a strong storm event in the inner-shelf of the Gulf of Lion (NW Mediterranean). Continent. Shelf Res. 25, 2410–2427.

Fischer, J., Visbeck, M., 1993. Deep velocity profiling with self-contained ADCPs. J. Atmos. Ocean. Technol. 10, 764–773.

Garau, B., Ruiz, S., Zhang, W.G., Pascual, A., Heslop, E., Kerfoot, J., Tintoré, J., 2011. Thermal lag correction on Slocum CTD glider data. J. Atmos. Ocean. Technol. 28, 1065–1071.

Gaudin, M., Berné, S., Jouanneau, J.-M., Palanques, A., Puig, P., Mulder, T., Cirac, P., Rabineau, M., Imbert, P., 2006. Massive sand beds attributed to deposition by dense water cascades in the Bourcart canyon head, Gulf of Lions (northwestern Mediterranean Sea). Mar. Geol. 234, 111–128.

Gentil, M., Many, G., Durrieu de Madron, X., Cauchy, P., Pairaud, I., Testor, P., Verney, R., Bourrin, F., 2020. Glider-based active acoustic monitoring of currents and turbidity in the coastal zone. Rem. Sens. 12, 2875.

Glenn, S., Jones, C., Twardowski, M., Bowers, L., Kerfoot, J., Kohut, J., Webb, D., Schofield, O., 2008. Glider observations of sediment resuspension in a Middle Atlantic Bight fall transition storm. Limnol. Oceanogr. 53, 2180–2196.

Glenn, S.M., Grant, W.D., 1987. A suspended sediment stratification correction for combined wave and current flows. J. Geophys. Res.: Oceans 92, 8244–8264. https://doi.org/10.1029/JC092iC08p08244.

Gordon, R.L., 1996. Acoustic Doppler current profiler-Principles of operation: a practical primer. Rd. Instruments 54, 54.

Gostiaux, L., van Haren, H., 2010. Extracting meaningful information from uncalibrated backscattered echo intensity data. J. Atmos. Ocean. Technol. 27, 943–949.

Got, H., Aloisi, J., 1990. The Holocene sedimentation on the Gulf of Lions margin: a quantitative approach. Continent. Shelf Res. 10, 841–855.

Grant, W.D., Madsen, O.S., 1979. Combined wave and current interaction with a rough bottom. J. Geophys. Res.: Oceans 84, 1797–1808.
Guillén, J., Bourrin, F., Palanques, A., De Madron, X.D., Puig, P., Buscail, R., 2006. Sediment dynamics during wet and dry storm events on the Têt inner shelf (SW Gulf of Lions). Mar. Geol. 234, 129–142.
Guillén, J., Soriano, S., Demestre, M., Falqués, A., Palanques, A., Puig, P., 2008. Alteration of bottom roughness by benthic organisms in a sandy coastal environment. Continent. Shelf Res. 28, 2382–2392.
Guizien, K., 2009. Spatial variability of wave conditions in the Gulf of Lions (NW mediterranean sea). Vie Milieu 59, 261.
Holmedal, L.E., Myrhaug, D., Rue, H., 2003. The sea bed boundary layer under random waves plus current. Continent. Shelf Res. 23, 717–750.
Jackett, D.R., McDougall, T.J., Feistel, R., Wright, D.G., Griffies, S.M., 2006. Algorithms for density, potential temperature, conservative temperature, and the freezing temperature of seawater. J. Atmos. Ocean. Technol. 23, 1709–1728.
Jia, L., Ren, J., Nie, D., Chen, B., Lv, X., 2014. Wave-current bottom shear stresses and sediment re-suspension in the mouth bar of the Modaomen Estuary during the dry season. Acta Oceanol. Sin. 33, 107–115.
Jing, L., Ridd, P.V., 1996. Wave-current bottom shear stresses and sediment resuspension in Cleveland Bay, Australia. Coast Eng. 29, 169–186.
Jordá, G., Bolaños, R., Espino, M., Sánchez-Arcilla, A., 2007. Assessment of the importance of the current-wave coupling in the shelf ocean forecasts. Ocean Sci. 3, 345–362.
Kane, I.A., Clare, M.A., 2019. Dispersion, accumulation, and the ultimate fate of microplastics in deep-marine environments: a review and future directions. Front. Earth Sci. 7 https://doi.org/10.3389/feart.2019.00080.
King, E., Conley, D., Masselink, G., Leonardi, N., McCarroll, R., Scott, T., 2019. The impact of waves and tides on residual sand transport on a sediment-poor, energetic, and macrotidal continental shelf. J. Geophys. Res.: Oceans 124, 4974–5002.
Liblik, T., Karstensen, J., Testor, P., Alenius, P., Hayes, D., Ruiz, S., Heywood, K., Pouliquen, S., Mortier, L., Mauri, Ejm, 2016. Potential for an underwater glider component as part of the global ocean observing system. Meth. Oceanography 17, 50–82.
Liu, X., Zhu, C., Zheng, J., Guo, L., Yin, P., Jia, Y., 2017. The observations of seabed sediment erosion and resuspension processes in the Jiaozhou Bay in China. Acta Oceanol. Sin. 36, 79–85.
Many, G., Bourrin, F., de Madron, X.D., Ody, A., Doxaran, D., Cauchy, P., 2018. Glider and satellite monitoring of the variability of the suspended particle distribution and size in the Rhône ROFI. Prog. Oceanogr. 163, 123–135.
Many, G., Bourrin, F., de Madron, X.D., Pairaud, I., Gangloff, A., Doxaran, D., Ody, A., Verney, R., Menniti, C., Le Berre, D., 2016. Particle assemblage characterization in the Rhone River ROFI. J. Mar. Syst. 157, 39–51.
Marsaleix, P., Auclair, F., Estournel, C., 2009. Low-order pressure gradient schemes in sigma coordinate models: the seamount test revisited. Ocean Model. 30, 169–177.
Marsaleix, P., Auclair, F., Estournel, C., 2006. Considerations on open boundary conditions for regional and coastal ocean models. J. Atmos. Ocean. Technol. 23, 1604–1613.
Marsaleix, P., Auclair, F., Floor, J.W., Herrmann, M.J., Estournel, C., Pairaud, I., Ulses, C., 2008. Energy conservation issues in sigma-coordinate free-surface ocean models. Ocean Model. 20, 61–89.
Marsaleix, P., Michaud, H., Estournel, C., 2019. 3D phase-resolved wave modeling with a non-hydrostatic ocean circulation model. Ocean Model. 136, 28–50.
Martín, J., Durrieu de Madron, X., Puig, P., Bourrin, F., Palanques, A., Houpert, L., Higueras, M., Sanchez-Vidal, A., Calafat, A.M., Canals, M., 2013. Sediment transport along the Cap de Creus Canyon flank during a mild, wet winter. Biogeosciences 10, 3221–3239.
McDougall, T.J., Barker, P.M., 2011. Getting started with TEOS-10 and the Gibbs Seawater (GSW) oceanographic toolbox. SCOR/IAPSO WG 127, 1–28.
McWilliams, J.C., Restrepo, J.M., 1999. The wave-driven ocean circulation. J. Phys. Oceanogr. 29, 2523–2540.
Michaud, H., Marsaleix, P., Leredde, Y., Estournel, C., Bourrin, F., Lyard, F., Mayet, C., Ardhuin, F., 2012. Three-dimensional modeling of wave-induced current from the surf zone to the inner shelf. Ocean Sci. 8, 657–681.
Mikolajczak, G., Estournel, C., Ulses, C., Marsaleix, P., Bourrin, F., Martín, J., Pairaud, I., Puig, P., Leredde, Y., Many, G., 2020. Impact of storms on residence times and export of coastal waters during a mild autumn/winter period in the Gulf of Lion. Continent. Shelf Res. 207, 104–192.
Miles, T., Glenn, S.M., Schofield, O., 2013. Temporal and spatial variability in fall storm induced sediment resuspension on the Mid-Atlantic Bight. Continent. Shelf Res. 63, S36—S49.
Miles, T., Seroka, G., Kohut, J., Schofield, O., Glenn, S., 2015. Glider observations and modeling of sediment transport in Hurricane Sandy. J. Geophys. Res.: Oceans 120, 1771–1791.
Miles, T., Slade, W., Glenn, S., 2021. Sediment resuspension and transport from a glider integrated Laser in Situ Scattering and Transmissometry (LISST) particle analyzer. J. Atmos. Ocean. Technol.
Miralles, J., Radakovitch, O., Aloisi, J.-C., 2005. 210Pb sedimentation rates from the Northwestern Mediterranean margin. Mar. Geol. 216, 155–167.
Monaco, A., 1971. Contribution à l'étude géologique et sédimentologique du plateau continental du Roussillon. Golfe du Lion).
Mullison, J., 2017. Backscatter estimation using broadband acoustic Doppler current profilers-updated. In: Presented at the Proceedings of the ASCE Hydraulic Measurements & Experimental Methods Conference, Durham, NH, USA, pp. 9–12.
Mullison, J., DeCollibus, C., Allsup, B., 2013. An investigation of the accuracy of current profile measurements from a glider-mounted ADCP operating in shallow water. In: Presented at the 2013 OCEANS-San Diego. IEEE, pp. 1–8.
Nielsen, P., 1992. Coastal Bottom Boundary Layers and Sediment Transport. World scientific.
Nittrouer, C.A., Austin, J.A.J.R., Field, M.E., Kravitz, J.H., Syvitski, J.P.M., Wiberg, P.L., 2007. Writing a rosetta stone: insights into continental-margin sedimentary processes and strata. In: Jarvis, I., Nittrouer, C.A., Austin, J.A., Field, M.E., Kravitz, J. H., Syvitski, J.P.M., Wiberg, P.L. (Eds.), Continental Margin Sedimentation. https://doi.org/10.1002/9781444304398.ch1.
Niu, J., Xu, J., Li, G., Dong, P., Shi, J., Qiao, L., 2020. Swell-dominated sediment re-suspension in a silty coastal seabed. Estuar. Coast Shelf Sci. 242 (106), 845.
Ogston, A., Sternberg, R., 1999. Sediment-transport events on the northern California continental shelf. Mar. Geol. 154, 69–82.
Ogston, A.S., Drexler, T.M., Puig, P., 2008. Sediment delivery, resuspension, and transport in two contrasting canyon environments in the southwest Gulf of Lions. Continent. Shelf Res. 28, 2000–2016.
Olsen, C.R., Cutshall, N.H., Larsen, I.L., 1982. Pollutant—particle associations and dynamics in coastal marine environments: a review. Mar. Chem. 11 (6), 501–533. https://doi.org/10.1016/0304-4203(82)90001-9.
Ordonez, C.E., Shearman, R.K., Barth, J.A., Welch, P., Erofeev, A., Kurokawa, Z., 2012. Obtaining Absolute Water Velocity Profiles from Glider-Mounted Acoustic Doppler Current Profilers. Presented at the 2012 Oceans-Yeosu, IEEE, pp. 1–7.
Palanques, A., de Madron, X.D., Puig, P., Fabres, J., Guillén, J., Calafat, A., Canals, M., Heussner, S., Bonnin, J., 2006. Suspended sediment fluxes and transport processes in the Gulf of Lions submarine canyons. The role of storms and dense water cascading. Mar. Geol. 234, 43–61.
Palanques, A., Guillén, J., Puig, P., de Madron, X.D., 2008. Storm-driven shelf-to-canyon suspended sediment transport at the southwestern Gulf of Lions. Continent. Shelf Res. 28, 1947–1956.
Palinkas, C., Ogston, A., Nittrouer, C., 2010. Observations of event-scale sedimentary dynamics with an instrumented bottom-boundary-layer tripod. Mar. Geol. 274, 151–164.
Peine, F., Bobertz, B., Graf, G., 2005. Influence of the blue mussel Mytilus edulis (Linnaeus) on the bottom roughness length (z0) in the south-western Baltic Sea. Baltica 18, 13–22.
Perez Belmonte, L., 2003. Enregistrement de la dernière transgression dans le Golfe du Lion. DEA Thesis. Univ. Lille 1, 52.
Perlin, A., Moum, J., Klymak, J., Levine, M., Boyd, T., Kosro, P., 2007. Organization of stratification, turbulence, and veering in bottom Ekman layers. J. Geophys. Res.: Oceans 112.
Petrenko, A., Dufau, C., Estournel, C., 2008. Barotropic eastward currents in the western Gulf of Lion, north-western Mediterranean Sea, during stratified conditions. J. Mar. Syst. 74, 406–428.
Prescott, P., Walden, A., 1980. Maximum likelihood estimation of the parameters of the generalized extreme-value distribution. Biometrika 67, 723–724.
Pruski, A.M., Buscail, R., Bourrin, F., Vétion, G., 2019. Influence of coastal Mediterranean rivers on the organic matter composition and reactivity of continental shelf sediments: the case of the Têt River (Gulf of Lions, France). Continent. Shelf Res. 181, 156–173.
Rosenberger, K.J., Storlazzi, C.D., Cheriton, O.M., 2016. Variability of the internal tide on the southern Monterey Bay continental shelf and associated bottom boundary layer sediment transport. Continent. Shelf Res. 120, 68–81.
Rudnick, D.L., 2016. Ocean research enabled by underwater gliders. Ann. Rev. Mar. Sci 8, 519–541.
Rudnick, D.L., Sherman, J.T., Wu, A.P., 2018. Depth-average velocity from Spray underwater gliders. J. Atmos. Ocean. Technol. 35, 1665–1673.
Sadaoui, M., Ludwig, W., Bourrin, F., Raimbault, P., 2016. Controls, budgets and variability of riverine sediment fluxes to the Gulf of Lions (NW Mediterranean Sea). J. Hydrol. 540, 1002–1015.
Schulz, A.C., Badewien, T.H., Garaba, S.P., Zielinski, O., 2016. Acoustic and optical methods to infer water transparency at time series station spiekeroog, wadden sea. Ocean Sci. 12 (6), 1155–1163.
Shi, J.Z., Wang, Y., 2008. The vertical structure of combined wave—current flow. Ocean Eng. 35, 174–181.
Simarro, G., Guillén, J., Puig, P., Ribó, M., Lo Iacono, C., Palanques, A., Muñoz, A., Durán, R., Acosta, J., 2015. Sediment dynamics over sand ridges on a tideless mid-outer continental shelf. Mar. Geol. 361, 25–40.
Soulsby, R., 1997. Dynamics of Marine Sands.
Soulsby, R.L., 1983. The Bottom Boundary Layer of Shelf Seas. Elsevier Oceanography Series. Elsevier, pp. 189–266.
Soulsby, R.L., Hamm, L., Klopman, G., Myrhaug, D., Simons, R., Thomas, G., 1993. Wave-current interaction within and outside the bottom boundary layer. Coast Eng. 21, 41–69.
Styles, R., Glenn, S.M., 2005. Long-term sediment mobilization at a sandy inner shelf site, LEO-15. J. Geophys. Res.: Oceans 110.
Styles, R., Glenn, S.M., 2000. Modeling stratified wave and current bottom boundary layers on the continental shelf. J. Geophys. Res.: Oceans 105, 24119–24139.
Testor, P., de Young, B., Rudnick, D.L., Glenn, S., Hayes, D., Lee, C.M., Pattiaratchi, C., Hill, K., Heslop, E., Turpin, V., 2019. OceanGliders: a component of the integrated GOOS. Front. Mar. Sci. 6, 422.
Tolman, H.L., 2009. User manual and system documentation of WAVEWATCH III TM version 3.14. Technical note. MMAB Contrib. 276, 220.
Troupin, C., Barth, A., Sirjacobs, D., Ouberdous, M., Brankart, J.-M., Brasseur, P., Rixen, M., Alvera-Azcárate, A., Belounis, M., Capet, A., 2012. Generation of analysis and consistent error fields using the Data Interpolating Variational Analysis (DIVA). Ocean Model. 52, 90–101.

Ulses, C., Estournel, C., Bonnin, J., Durrieu de Madron, X., Marsaleix, P., 2008a. Impact of storms and dense water cascading on shelf-slope exchanges in the Gulf of Lion (NW Mediterranean). J. Geophys. Res.: Oceans 113.
Ulses, C., Estournel, C., De Madron, X.D., Palanques, A., 2008 b. Suspended sediment transport in the Gulf of Lions (NW Mediterranean): impact of extreme storms and floods. Continent. Shelf Res. 28, 2048–2070.
Van Rijn, L.C., Kroon, A., 1993. Sediment transport by currents and waves. In: Coastal Engineering 1992, pp. 2613–2628.
Van Sebille, E., Aliani, S., Law, K.L., Maximenko, N., Alsina, J.M., Bagaev, A., Bergmann, M., Chapron, B., Chubarenko, I., Cózar, A., 2020. The physical oceanography of the transport of floating marine debris. Environ. Res. Lett. 15, 023003.
Weaver, P., Canals, M., Trincardi, F., 2006. EUROSTRATAFORM vol 1: source to sink sedimentation on the European margin. Special issue of marine geology. Mar. Geol. 234, 1–292.
Xu, J., Wright, L., 1995. Tests of bed roughness models using field data from the Middle Atlantic Bight. Continent. Shelf Res. 15, 1409–1434.
Xu, Z., Bowen, A., 1994. Wave-and wind-driven flow in water of finite depth. J. Phys. Oceanogr. 24, 1850–1866.